

**Photoproduction
of ω Mesons off Protons
with Linearly Polarized Photons**

F.J. Klein^{*†‡}, V. Burkert, E.S. Smith

Thomas Jefferson National Accelerator Facility, Newport News, VA 23606

P.L. Cole^{*}

University of Texas at El Paso, El Paso, TX 79968

J.C. Sanabria

Universidad de los Andes, Bogotá, Colombia

H. Crannell, D.I. Sober

The Catholic University of America, Washington, DC 20064

H. Funsten

College of William and Mary, Williamsburg, VA 23185

C. Bennhold, B.L. Berman, W.J. Briscoe, K.S. Dhuga, I. Strakovsky

The George Washington University, Washington, DC 20052

Z.P. Li, Q. Zhao

Peking University, Beijing 100871, PR China

S. Capstick

Florida State University, Tallahassee, FL 32306

W. Roberts

Old Dominion University, Norfolk, VA 23529

J.-P. Didelez, M. Guidal, E. Hourany

Institut de Physique Nucléaire, Université de Paris, Orsay, France

J.-M. Laget

CEA-Saclay, DAPNIA/SPhN, Gif-sur-Yvette, France

J.D. Kellie, K. Livingston, D. Ireland, R.O. Owens, G. Rosner

Glasgow University, Glasgow, Great Britain

+

The CLAS Collaboration

* Co-Spokesperson

† Contact person

‡ Will present proposal

Abstract

The photoproduction of ω mesons off protons will be used to study baryon resonances and t -exchange processes in the center-of-mass energy regime of 1.73 to 2.24 GeV. In baryon spectroscopy, the ωN channel is expected to be a significant branch for the decay of baryon resonances carrying the isospin $I = \frac{1}{2}$. t -channel exchange contributions can only be disentangled by use of a linearly polarized photon beam. The measurement will employ a linearly polarized beam of photons produced by the approved Coherent Bremsstrahlung Facility to measure the beam asymmetry and the spin density matrix elements of the three-pion decay of the ω . The spin density matrix elements and polarization asymmetry of the ω decay will be extracted as functions of the center-of-mass energy \sqrt{s} and the ω production angle θ_{cm} in the center-of-mass frame. These measurements will expedite the search for baryon resonance contributions and will provide new physics information on diffractive, t - and u -channel processes. The proposed experiment will probe the lower energy region ($1.2 < E_\gamma < 1.6$ GeV) with an average photon polarization of 65% by using a 4 GeV electron beam. A second run with a 6 GeV electron beam will permit measurements in the energy regime $1.5 < E_\gamma < 2.2$ GeV with an average photon polarization of 80%. The 100 MeV overlap will allow for cross checking and comparing the results of the two runs. We propose to collect data in parallel with and contiguous to the already approved experiments E94-109 and E98-109, which are scheduled for the $\gamma 8$ CLAS running period.

1 Introduction

We propose to measure the production of ω mesons by using a beam of linearly polarized photons. The measurement of the complete angular distributions of the decay products of the ω will result in a set of rigid constraints necessary for elucidating the character of the exchange between the target nucleon and the incident photon for low four-momentum transfer squared t , and provide crucial information on the extraction of masses, partial widths, and helicity amplitudes of baryon resonances that decay via the ωN mode. Due to the narrow decay width (8.43 MeV) of the ω meson and to isospin selectivity, the ω meson channel will serve as a unique signal for extracting N^* resonances that possess an isospin of $1/2$. The quantities to be measured in this experiment are the spin density matrix elements of the ω . These observables, three from unpolarized photoproduction experiments and six additional ones with a linearly polarized photon beam, are extracted in the rest frame of the ω by measuring the polar and azimuthal angular distributions of the decay pions referenced with respect to the orientation of the photon spin. Data to be obtained over the full θ_{lab} range and over a large incident photon energy range will allow us to extract the spin density matrix elements as functions both of the c.m. energy \sqrt{s} and of the c.m. polar angle θ_{cm} between the beam axis and the produced ω meson. By using CLAS, the photon tagger and a continuous electron beam, we will be able to perform these measurements with full angular coverage, low systematic uncertainties, and high statistics.

Linearly polarized photons at high energies have been used to determine the natural parity character of the pomeron exchange in the Vector Meson Dominance model (VMD). The ω photoproduction data [1] in the energy range of $20 < E_\gamma < 70$ GeV, in particular, has lent strong support to VMD. From the SLAC bubble-chamber experiment using a linearly polarized beam of photons with $E_\gamma = 2.8$ and 4.7 GeV, large contributions of unnatural-parity exchange were measured for ω photoproduction [2]. Such behavior is expected in models which are based upon one-pion exchange ($J^\pi = 0^-$) in the t -channel [3], [4]. The strength of the contributions from either natural- or unnatural-parity exchange can be determined by the density matrix elements. All but two of the nine measureable matrix elements are zero for both of these processes, and a flip in sign of one of these observables allows one to distinguish between natural- and unnatural-parity exchange.

At resonance energies ($\sqrt{s} < 2.4$ GeV), the high energy approximation used to sepa-

rate natural- and unnatural-parity exchange no longer holds over the whole t -range. Instead, s -channel processes may contribute as well. Unlike diffractive ω photoproduction, the helicity of the photon is not directly transferred to the ω meson. We expect to see a much different behavior of the spin density matrix elements at energies where resonance contributions are important compared with higher energies.

Whereas diffractive and t -channel exchange contributions will dominate the ω cross section at low t , and u -channel exchange will be large at high t , we expect the contributions from resonance production to be enhanced in the mid- t regime. The low- and high- t processes are of interest in their own right, and interference effects with resonant ω photoproduction may well be significant. We will be measuring over the full kinematical range in t and thus will be sensitive to all of these processes. Furthermore, the probe of linearly polarized photons provides a powerful tool for disentangling the contributions of natural-parity (Pomeron, σ , f_2) and unnatural-parity exchange (mostly pion) in the t -channel.

2 Motivation

The spectrum of excited states of a system of bound particles opens a window to the underlying interaction. Just as in nuclear spectroscopy, where the excited-state spectrum reflects the quantum many-body configurations of nucleons and mesons interacting via the strong nuclear force, so does baryon spectroscopy afford us the opportunity to study the interaction of quarks and gluons in excited states.

An important motivation for studying the spectrum of baryon resonances with photons is to obtain information on the photoproduction amplitudes of the individual resonances. Most of our knowledge of the baryon resonance spectrum has come from the reactions $\pi N \rightarrow \pi N$, $\gamma N \rightarrow \pi N$, and $\pi N \rightarrow \pi\pi N$. At center-of-mass energies below 1.7 GeV, the single pion production channel dominates both the pion and photoabsorption cross sections. As the c.m. energy increases towards 2.0 GeV, the two- and three-pion decay channels become dominant, and it is in this energy region that the masses and partial widths of the resonances are poorly determined.

An outstanding problem in our understanding of baryon spectroscopy is that of the

missing resonances. For example, $SU(6) \otimes O(3)$ symmetric quark models predict far more resonances than have been observed. One solution is to restrict the number of internal degrees of freedom by assuming that two quarks are bound in a diquark pair [5], thus lowering the level density of baryon resonances. An alternate solution has been put forward by Koniuk and Isgur [6] and others [7],[8]. In these calculations, it was found that the missing resonances tend to couple weakly to the πN channel but stronger to the ρN , $\pi\Delta$, and ωN channels. For example, in Table 1, we tabulate the supermultiplet assignments with the corresponding PDG [9] star rating for the measured and missing baryon resonances from the QCD-improved model of Cutkosky [10]. The supermultiplets in the boxes are fully consistent with the predictions of the diquark model. We remark that all of the boxed entries have at least a three-star rating. We also observe that the positive parity P11(1710) and P13(1870) resonances are inconsistent with the diquark model. The partial widths for the photon and hadronic couplings in the framework of Koniuk-Isgur are contained in Table 2. We note that the P13(1870) as well as the F15(1955) are predicted to have primarily an ωN decay mode. Since most of our information on the baryon resonance spectrum comes from partial-wave analyses of $\pi N \rightarrow \pi N$ measurements, these ‘missing states’ will clearly have escaped detection. The models predict that these resonances will have a reasonable coupling to the photon. For this reason, an approved CEBAF experiment [11] using unpolarized electrons will search for resonances decaying via the ωN channel. We expect the identification of many of these resonances decaying through the ωN mode to be difficult due to their broad widths and narrow spacing. The sensitivity afforded by linearly polarized photons will provide additional constraints in identifying these resonances, and such a measurement is complementary to electroproduction experiments.

Experimentally, several difficulties are apparent. The number of resonances extracted either from the analyses of pion production data or from the theoretical predictions is large. In addition, the resonance widths are broad (typically ~ 150 MeV), and one is faced with the problem of disentangling many overlapping resonances. Moreover, diffractionlike processes dominate the vector meson photoproduction in forward angles. A phase-shift analysis is required to identify resonant behaviour and to extract the helicity amplitudes for the various resonances. Such an analysis is greatly supported by the measurement of polarization observables.

Table 1: $SU(6) \otimes O(3)$ supermultiplet assignments from the QCD-improved model of Cutkosky for the measured and *missing* baryon resonances. The boxed supermultiplets are fully consistent with the diquark model.

N^*	Status	$SU(6) \otimes O(3)$	Parity	Δ^*	Status	$SU(6) \otimes O(3)$
P11(938)	****	$(56, 0^+)$	+	P33(1232)	****	$(56, 0^+)$
S11(1535)	****	$(70, 1^-)$	—	S31(1620)	****	$(70, 1^-)$
S11(1650)	****	$(70, 1^-)$		D33(1700)	****	$(70, 1^-)$
D13(1520)	****	$(70, 1^-)$				
D13(1700)	***	$(70, 1^-)$				
D15(1675)	****	$(70, 1^-)$				
P11(1520)	****	$(56, 0^+)$		P31(1875)	****	$(56, 2^+)$
P11(1710)	***	$(70, 0^+)$		P31(1835)		$(70, 0^+)$
P11(1880)		$(70, 2^+)$				
P11(1975)		$(20, 1^+)$				
P13(1720)	****	$(56, 2^+)$	+	P33(1600)	***	$(56, 0^+)$
P13(1870)	*	$(70, 0^+)$		P33(1920)	***	$(56, 2^+)$
P13(1910)		$(70, 2^+)$		P33(1985)		$(70, 2^+)$
P13(1950)		$(70, 2^+)$				
P13(2030)		$(20, 1^+)$				
F15(1680)	****	$(56, 2^+)$		F35(1905)	****	$(56, 2^+)$
F15(2000)	**	$(70, 2^+)$		F35(2000)	**	$(70, 2^+)$
F15(1995)		$(70, 2^+)$				
F17(1990)	**	$(70, 2^+)$		F37(1950)	****	$(56, 2^+)$

Table 2: Partial widths for photon and hadronic couplings to baryon resonances in the Isgur-Karl model. The total hadronic width, summed over all identified channels, is also given. The units are MeV.

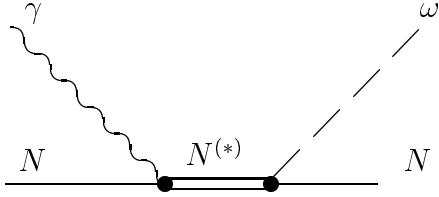
Mass	J^π	γp	πN	$\pi \Delta$	ρN	ωN	Total
N(1490)	$1/2^-$	1.3	28.	2.9	40.	0.	98.
N(1655)	$1/2^-$	0.72	76.	67.	102.	1.4	262.
N(1535)	$1/2^-$	0.58	85.	52.	27.	0.	164.
N(1745)	$3/2^-$	0.009	13.	317.	26.	2.9	360.
N(1670)	$5/2^-$	0.013	30.	86.	5.3	0.	130.
N(1405)	$1/2^+$	0.026	46.	5.8	0.1	0.	52.
N(1705)	$1/2^+$	0.23	45.	13.	36.	0.8	108.
N(1890)	$1/2^+$	0.057	19.	12.	22.	37.	96.
N(2055)	$1/2^+$	0.009	1.4	3.2	1.7	32.	39.
N(1710)	$1/2^+$	1.0	42.	4.4	156.	32.	242.
N(1870)	$3/2^+$	0.027	10.	19.	2.3	98.	149.
N(1955)	$3/2^+$	0.021	1.2	88.	56.	90.	236.
N(1980)	$3/2^+$	0.031	1.2	96.	71.	55.	223.
N(2060)	$3/2^+$	0.0001	0.3	31.	15.	98.	145.
N(1715)	$5/2^+$	0.29	50.	4.4	20.	1.4	77.
N(1955)	$5/2^+$	0.24	0.2	64.	67.	184.	324.
N(2025)	$5/2^+$	0.001	1.7	67.	66.	180.	316.
N(1955)	$7/2^+$	0.006	9.6	36.	18.	53.	126.
$\Delta(1685)$	$1/2^-$	0.34	11.	64.	64.	--	139.
$\Delta(1685)$	$3/2^-$	1.0	24.	146.	289.	--	459.
$\Delta(1925)$	$1/2^+$	0.0	28.	35.	37.	--	112.
$\Delta(1240)$	$3/2^+$	0.46	121.	0.	0.	--	121.
$\Delta(1780)$	$3/2^+$	0.14	29.	74.	32.	--	139.
$\Delta(1975)$	$3/2^+$	0.030	0.	59.	35.	--	94.
$\Delta(1940)$	$5/2^+$	0.059	16.	41.	45.	--	103.
$\Delta(1975)$	$5/2^+$	0.51	1.	41.	388.	--	430.
$\Delta(1915)$	$7/2^+$	0.27	56.	30.	88.	--	178.

3 Physics

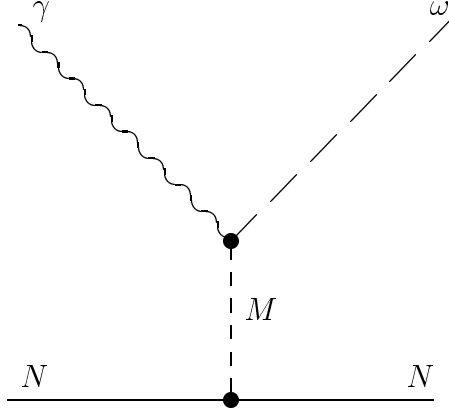
3.1 Processes Contributing to ω Photoproduction

From the duality principle, the cross section for ω photoproduction can be calculated, in principle, by summing over all possible t -channel meson-exchange processes [Fig. 1(b)], or over all possible s -channel *plus* all possible u -channel baryon-exchange processes. The pomeron exchange contribution to diffractive scattering of Fig. 1(d) needs to be added as a special case, as the effects of pomeron exchange in the t -channel are understood to be in addition to those of meson exchange. In the diffractive (low- t) region, it is more efficient to sum over t -channel exchange processes, the sum over s -channel plus u -channel processes would require a large number of intermediate baryon states for convergence. Similarly, in the resonance region a t -channel sum will yield only the average cross section and will not show the characteristic energy dependence attributed to baryon resonances.

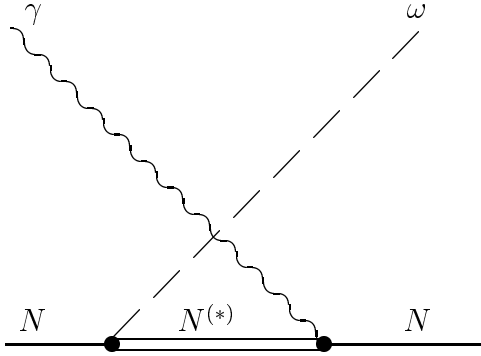
Constructing the cross section from a model, and likewise extracting resonance parameters from an analysis of the cross section, will therefore require different approaches in different kinematical regions. The s -channel sum used for an estimate of the resonance region cross section needs to be supplemented by the terms representing the u -channel diagrams of Fig. 1(c). If we work within time-ordered perturbation theory, in lowest order, these diagrams will be suppressed relative to the s -channel diagrams because of energy denominators which are increased by the presence of the initial photon and the final ω in the intermediate state. For a given intermediate baryon resonance, the \sqrt{s} for which the denominator is minimized, is pushed up to a higher value, and the minimum attained is significantly larger, relative to the s -channel diagram.



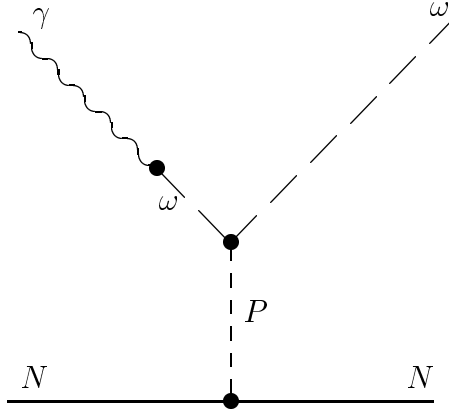
(a) s -channel baryon exchange



(b) t -channel meson exchange



(c) u -channel baryon exchange



(d) diffractive scattering via
Pomeron exchange

Figure 1: Processes involved in ω -meson photoproduction.

3.2 The Decay Angular Distribution

The goal of the proposed experiment is to measure the reaction $\gamma p \rightarrow \omega p$ by using a linearly polarized photon beam in the energy range of $1.1 \leq E_\gamma \leq 2.2$ GeV. In a practical sense, we will be measuring the angular momenta and thus the spin density matrix elements $\rho_{\alpha\beta}^j$, which describe the polarization states of the ω meson and thereby determine the angular distribution $W(\cos \theta, \phi, \Phi)$ of the three decay pions. The upper index (j) is related to photon spin by the Pauli spin matrices, the lower indices, $\alpha, \beta = -1, 0, 1$, correspond to the possible helicity states of the vector meson. The complete angular distribution reads [12]:

$$\begin{aligned} W(\cos \theta, \phi, \Phi) = & W^0(\cos \theta, \phi, \rho_{\alpha\beta}^0) - P_\gamma \cos 2\Phi W^1(\cos \theta, \phi, \rho_{\alpha\beta}^1) \\ & - P_\gamma \sin 2\Phi W^2(\cos \theta, \phi, \rho_{\alpha\beta}^2) \\ & + \lambda_\gamma P_\gamma W^3(\cos \theta, \phi, \rho_{\alpha\beta}^3). \end{aligned} \quad (1)$$

where,

$$\begin{aligned} W^0(\cos \theta, \phi, \rho_{\alpha\beta}^0) = & \frac{3}{4\pi} \left[\frac{1}{2} \sin^2 \theta + \frac{1}{2} (3 \cos^2 \theta - 1) \rho_{00}^0 \right. \\ & \left. - \sqrt{2} \operatorname{Re} \rho_{10}^0 \sin 2\theta \cos \phi - \rho_{1-1}^0 \sin^2 \theta \cos 2\phi \right], \end{aligned} \quad (2)$$

$$\begin{aligned} W^1(\cos \theta, \phi, \rho_{\alpha\beta}^1) = & \frac{3}{4\pi} \left[\rho_{11}^1 \sin^2 \theta + \rho_{00}^1 \cos^2 \theta \right. \\ & \left. - \sqrt{2} \operatorname{Re} \rho_{10}^1 \sin 2\theta \cos \phi - \rho_{1-1}^1 \sin^2 \theta \cos 2\phi \right], \end{aligned} \quad (3)$$

$$W^2(\cos \theta, \phi, \rho_{\alpha\beta}^2) = \frac{3}{4\pi} \left[\sqrt{2} \operatorname{Im} \rho_{10}^2 \sin 2\theta \sin \phi + \operatorname{Im} \rho_{1-1}^2 \sin^2 \theta \sin 2\phi \right], \quad (4)$$

$$W^3(\cos \theta, \phi, \rho_{\alpha\beta}^3) = \frac{3}{4\pi} \left[\sqrt{2} \operatorname{Re} \rho_{10}^3 \sin 2\theta \sin \phi + \operatorname{Im} \rho_{1-1}^3 \sin^2 \theta \sin 2\phi \right]. \quad (5)$$

Here,

$W^0(\cos \theta, \phi)$ describes the decay distribution for an unpolarized photon beam,

$W^0(\cos \theta, \phi)$, $W^1(\cos \theta, \phi)$, and $W^2(\cos \theta, \phi)$ for a linearly polarized beam, and

$W^0(\cos \theta, \phi)$ and $W^3(\cos \theta, \phi)$ for a circularly polarized beam with a photon helicity λ_γ .

P_γ is the degree of polarization of the photon beam, Φ the angle of photon polarization vector with respect to the production plane. The angles θ and ϕ are the polar and azimuthal angles of the normal to the ω decay plane with respect to a quantization axis z in the production plane. Depending upon what information one wishes to extract, one selects that reference frame which allows for the simplest representation of the density matrices.

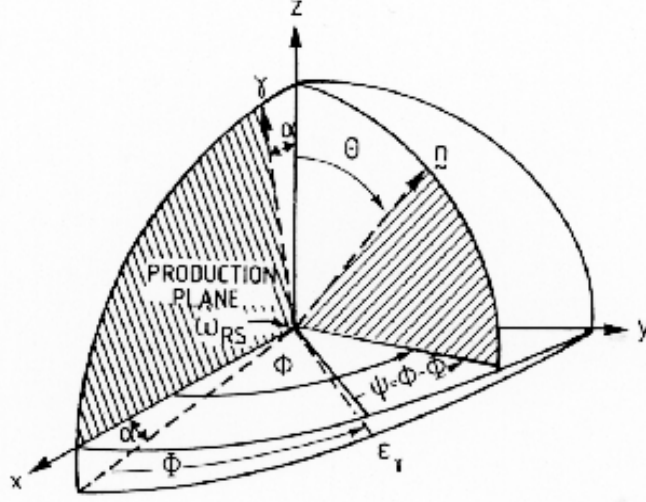


Figure 2: Helicity reference frame. Φ is the azimuthal angle of the electric vector \vec{E}_γ of the photon, and θ and ϕ are the polar and azimuthal angles of the normal to the decay plane defined by $\vec{p}_{\pi^+} \times \vec{p}_{\pi^-}$.

For example, in the helicity frame the density matrices reduce to an elementary form for natural-parity exchange processes, and the Gottfried-Jackson frame is well suited for 0^\pm processes. The transversity frame, in general, provides a simple form for these observables when calculating polarization observables.¹ Shown in Fig. 2 is the graphical depiction of these angles.

With linearly polarized photons, one has access to six more independent spin density matrix elements than can be obtained in an unpolarized vector meson photoproduction experiment. By using CLAS, we will measure the angular distribution (and hence the spin density matrix elements) of ω production both as a function of the c.m. energy \sqrt{s} and of the ω production angle θ_{cm} .

At high photon energies the measured density matrix elements give rise to an angular dependence that is characteristic of natural-parity exchange (pomeron exchange) in the t -channel and of s -channel helicity conservation (SCHC), as one would expect if the helicity of the vector meson reflects that of the real photon. Shown in Fig. 3 are the angular

¹These reference frames differ by the definition of the quantization axis z , and can be transformed, one to the other, by appropriate rotations and Lorentz boosts. In the helicity frame the z -axis is defined as the direction opposite to the outgoing proton in the total c.m. system; in the Gottfried-Jackson frame, the z -axis is defined as the direction of the incoming photon in the rest frame of the ω , whereas in the Adair frame, the z -axis is defined as the direction of the incoming photon in the total c.m. system; it differs from the helicity frame by a rotation of the angle α in Fig. 2. In the transversity frame, the quantization axis is defined as the normal of the production plane.

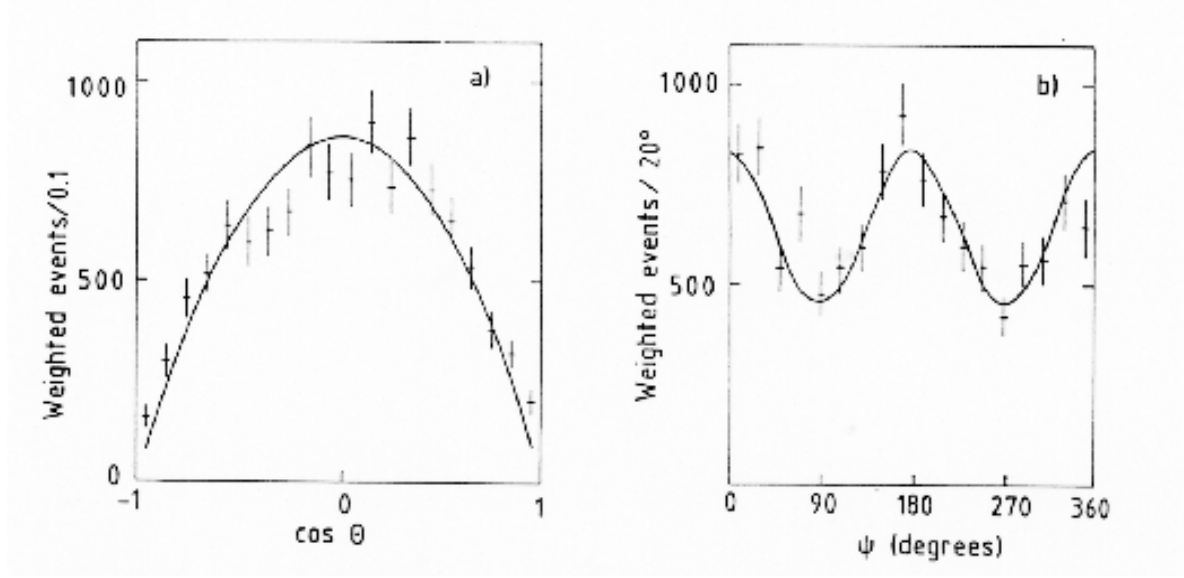


Figure 3: Linearly polarized photon data ($\gamma p \rightarrow \omega p$) from CERN [1] showing the angular distribution of the data as functions of helicity polar angle $\cos(\theta_{hel})$ and Ψ as defined in the text.

distributions for events in the ω mass range as observed by the OMEGA collaboration [1]. The experiment used a beam of linearly polarized photons in the energy range between 20 and 70 GeV, with a mean polarization of 48%. The data are displayed as a function of $\cos \theta_{hel}$ and as a function of $\Psi = \phi_{hel} - \Phi$ (with θ_{hel} , ϕ_{hel} , and Φ as defined in Fig. 2). For a polarization of unity ($P_\gamma = 1$), s -channel helicity conservation demands that the three pions from the ω decay have an angular distribution given by $\sin^2 \theta_{hel} \cos 2\psi_{hel}$, and this is reflected in the data. The decay products from the ω decay lie preferentially in the plane where Φ , the angle made by the photon electric polarization vector and the production plane, is equal to the azimuthal decay angle.

Another way to determine this feature is to measure the photon asymmetry parameter

$$\Sigma \equiv \frac{\sigma_{\parallel} - \sigma_{\perp}}{\sigma_{\parallel} + \sigma_{\perp}}.$$

Here σ_{\parallel} (σ_{\perp}) is the cross section for the pions from ω decay ($\theta = \pi/2, \phi = \pi/2$), to emerge in the plane of the photon polarization (or perpendicular to it). In terms of the decay distribution and the measurable density matrix elements Σ can be rewritten as

$$\Sigma = \frac{W(\cos \frac{\pi}{2}, \frac{\pi}{2}, \frac{\pi}{2}) - W(\cos \frac{\pi}{2}, \frac{\pi}{2}, 0)}{W(\cos \frac{\pi}{2}, \frac{\pi}{2}, \frac{\pi}{2}) + W(\cos \frac{\pi}{2}, \frac{\pi}{2}, 0)} = P_\gamma \frac{2(\rho_{11}^1 + \rho_{1-1}^1)}{1 - \rho_{00}^0 + 2\rho_{1-1}^0}. \quad (6)$$

If helicity is conserved in the s -channel, then only two of the nine density matrix elements are nonzero: $\rho_{1-1}^1 = 0.5$, $\text{Im}\rho_{1-1}^2 = -0.5$, hence $\Sigma=1$ when $P_\gamma=1$ (with θ, ϕ determined in the

helicity frame). Any deviation from this value is an indication that nondiffractive processes are present. Likewise, the analysis of angular momenta in the Gottfried-Jackson frame reflects helicity conservation in the t channel in the case that all matrix elements are zero except $\rho_{11}^1 = -\text{Im } \rho_{1-1}^2 = 0.5$.

Furthermore, the analysis of the density matrices provides insight into character of exchange processes in the t channel. The exchange of pseudoscalar mesons carries unnatural parity ($J^\pi = 0^-$) while the exchange of Pomeron, scalar, or tensor mesons imply natural parity ($J^\pi = 0^+, 2^+$). The corresponding parity asymmetry parameter P_σ is defined as

$$P_\sigma = \frac{\sigma^{(n)} - \sigma^{(u)}}{\sigma^{(n)} + \sigma^{(u)}} ,$$

which can be recast in terms of the density matrix elements as

$$P_\sigma = 2\rho_{1-1}^1 - \rho_{00}^1 . \quad (7)$$

If the production mechanisms carry only natural parity, then $P_\sigma = 1$ ($\rho_{1-1}^1 = 0.5$, $\rho_{00}^1 = 0$). Purely unnatural-parity exchange is indicated by $P_\sigma = -1$ ($\rho_{1-1}^1 = -0.5$, $\rho_{00}^1 = 0$). An intermediate asymmetry value can be decomposed into its constituent contributions. We should remark that this flipping of the parity asymmetry is valid only if no additional processes other than t -exchange mechanisms contribute. We will apply this to ω photoproduction in the low- t range, where contributions primarily from one-pion exchange (unnatural parity) as well as Pomeron, scalar- and tensor-meson processes (natural parity) are expected to dominate the differential cross section.

We performed calculations within the framework of Regge theory [13], which describe well both the high energy and the low energy ω photoproduction data (cf. Fig. 4). The Pomeron trajectory contributes little to ω production near threshold. In this energy regime, one-pion exchange dominates the cross section, with contributions from f_2 exchange having a significant strength as well. The experimental data points reflect the world's data set covering early experiments at SLAC and DESY ($W < 7$ GeV), CERN and FNAL (W around 10-20 GeV), and the present HERA experiments ($W \approx 81$ GeV).

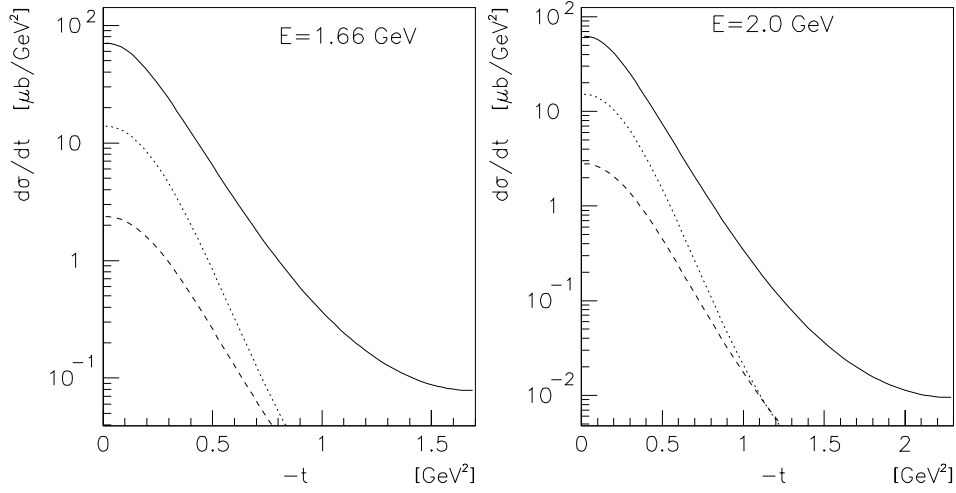
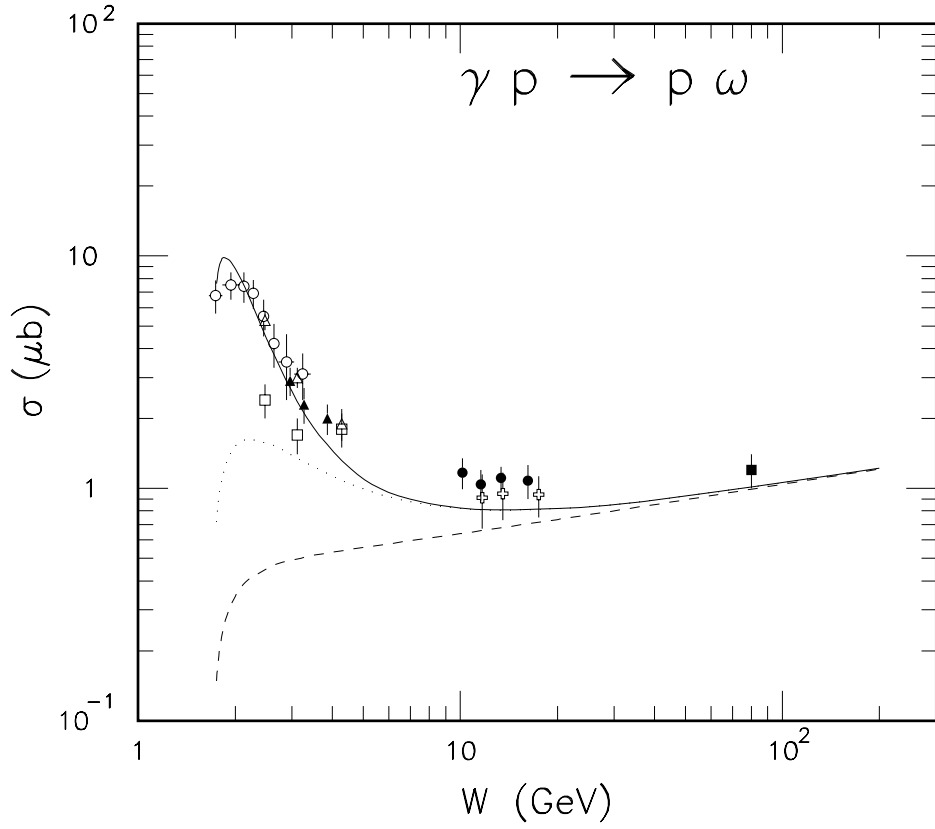


Figure 4: Regge calculations by J.M. Laget of the ω cross section incorporating the processes: Pomeron trajectory (*dashed line*), Pomeron plus f_2 exchange (*dotted line*), Pomeron plus f_2 plus π exchange (*solid line*) in the t -channel. The experimental data points in the top figure are the world's data set (SLAC, DESY, CERN, FNAL, and HERA).

3.3 Density Matrix Elements and Helicity Amplitudes

The basic amplitude \mathcal{F} for processes $\gamma N \rightarrow VN'$ is defined as

$$\mathcal{F} = \langle \mathbf{q} \lambda_V \lambda_{N'} | T | \mathbf{k} \lambda_\gamma \lambda_N \rangle,$$

where \mathbf{k} and \mathbf{q} are the momenta of the incoming photon and outgoing vector meson, respectively. The helicity states are denoted by $\lambda_\gamma = \pm 1$ for the incoming photon, $\lambda_V = 0, \pm 1$ for the outgoing vector meson, and $\lambda_N = \pm 1/2, \lambda_{N'} = \pm 1/2$ for the initial and final state nucleons, respectively. Following Ref. [14], the amplitude \mathcal{F} can be expressed as a 6×4 matrix in the helicity space:

$$\mathcal{F} = \begin{pmatrix} H_{21} & H_{11} & H_{3-1} & -H_{4-1} \\ H_{41} & H_{31} & -H_{1-1} & -H_{4-1} \\ H_{20} & H_{10} & -H_{30} & H_{2-1} \\ H_{40} & H_{30} & H_{10} & H_{40} \\ H_{2-1} & H_{1-1} & H_{31} & -H_{41} \\ H_{4-1} & H_{3-1} & -H_{11} & H_{21} \end{pmatrix}. \quad (8)$$

Because of parity conservation the $H_{i\lambda_V}$ in equ. (8) reduces to 12 independent complex helicity amplitudes:

$$\begin{aligned} H_{1\lambda_V} &= \langle \lambda_V, \lambda_{N'} = +1/2 | T | \lambda_\gamma = 1, \lambda_N = -1/2 \rangle \\ H_{2\lambda_V} &= \langle \lambda_V, \lambda_{N'} = +1/2 | T | \lambda_\gamma = 1, \lambda_N = +1/2 \rangle \\ H_{3\lambda_V} &= \langle \lambda_V, \lambda_{N'} = -1/2 | T | \lambda_\gamma = 1, \lambda_N = -1/2 \rangle \\ H_{4\lambda_V} &= \langle \lambda_V, \lambda_{N'} = -1/2 | T | \lambda_\gamma = 1, \lambda_N = +1/2 \rangle \end{aligned} \quad (9)$$

In the spin space, the reaction $\gamma N \rightarrow VN'$ is expressed by a correlation between the initial and final state density matrices via the helicity amplitude matrix:

$$\rho_f = \mathcal{F} \rho_i \mathcal{F}^\dagger, \quad \text{where } \rho_f = \rho_V \times \rho_{N'}, \rho_i = \rho_\gamma \times \rho_N. \quad (10)$$

$\rho_\gamma, \rho_N, \rho_V, \rho_{N'}$ are the density matrices describing the polarization state of each particle:

$$\begin{aligned} \rho_\gamma &= \frac{I_\gamma}{2} (1_\gamma + \vec{\sigma}_\gamma \cdot \vec{P}_S), & \rho_N &= \frac{I_N}{2} (1_N + \vec{\sigma}_N \cdot \vec{P}_N), \\ \rho_{N'} &= \frac{I_{N'}}{2} (1_{N'} + \vec{\sigma}_{N'} \cdot \vec{P}_{N'}), & \rho_V &= \frac{I_V}{3} (1_V + \vec{S} \cdot \vec{P}_V + 3\tau \cdot T_V). \end{aligned} \quad (11)$$

\vec{P}_S is the Stokes' Vector which defines the photon polarization, \vec{P}_N is the target polarization vector, $\vec{P}_{N'}$ the recoil nucleon polarization vector, and \vec{P}_V and T_V are the vector polarization

and the tensor polarization of the vector meson, respectively. The density matrix elements as used in equ. (1) are formed of bilinear combinations of these amplitudes:

$$\begin{aligned}
\rho_{ik}^0 &= \frac{1}{A} \sum_{\lambda_\gamma \lambda_N \lambda_{N'}} H_{\lambda_{V_i} \lambda_{N'}, \lambda_\gamma \lambda_N} H_{\lambda_{V_k} \lambda_{N'}, \lambda_\gamma \lambda_N}^*, \\
\rho_{ik}^1 &= \frac{1}{A} \sum_{\lambda_\gamma \lambda_N \lambda_{N'}} H_{\lambda_{V_i} \lambda_{N'}, -\lambda_\gamma \lambda_N} H_{\lambda_{V_k} \lambda_{N'}, \lambda_\gamma \lambda_N}^*, \\
\rho_{ik}^2 &= \frac{1}{A} \sum_{\lambda_\gamma \lambda_N \lambda_{N'}} \lambda_\gamma H_{\lambda_{V_i} \lambda_{N'}, -\lambda_\gamma \lambda_N} H_{\lambda_{V_k} \lambda_{N'}, \lambda_\gamma \lambda_N}^*, \\
\rho_{ik}^3 &= \frac{1}{A} \sum_{\lambda_\gamma \lambda_N \lambda_{N'}} \lambda_\gamma H_{\lambda_{V_i} \lambda_{N'}, \lambda_\gamma \lambda_N} H_{\lambda_{V_k} \lambda_{N'}, \lambda_\gamma \lambda_N}^*,
\end{aligned} \tag{12}$$

where, $A = \sum_{\lambda_{V_i} \lambda_\gamma \lambda_N \lambda_{N'}} H_{\lambda_{V_i} \lambda_{N'}, \lambda_\gamma \lambda_N} H_{\lambda_{V_i} \lambda_{N'}, \lambda_\gamma \lambda_N}^*$.

Here, ρ_{ik} represents $\rho_{\lambda_{V_i} \lambda_{V_k}}$. The angular distribution of the decay particles of the vector meson is described by

$$W(\cos \theta, \phi, \Phi) \equiv \frac{dN}{d \cos \theta d\phi d\Phi} = M \rho_V M^\dagger$$

here, M denotes the decay amplitude which is given by a related mixture of Wigner d-functions; in the case of a decay into spinless particles it reads:

$$< \theta \phi | M | \lambda_V > = C \sqrt{\frac{3}{4\pi}} d_{\lambda_V 0}^1.$$

In order to determine the contributions of individual resonances, we will use a partial wave expansion of the helicity amplitudes:

$$h_{i\lambda_V}^J = < \mathbf{q} \lambda_V \lambda_{N'} | T^J | \mathbf{k} \lambda_\gamma \lambda_N >,$$

where the set of helicity quantum numbers for each i label ($i=1\dots 4$) is the same as in equ. (9). The partial wave helicity amplitudes $h_{i\lambda_V}^J$ are related to the helicity amplitude $H_{i\lambda_V}$ by:

$$H_{i\lambda_V} = \sum_{JM} \frac{2J+1}{4\pi} d_{M\Lambda_f}^{(J)*}(\mathbf{q}) d_{M\Lambda_i}^{(J)}(\mathbf{k}) h_{i\lambda_V}^J,$$

where, $\Lambda_f = \lambda_V - \lambda_{N'}$ and $\Lambda_i = \lambda_\gamma - \lambda_N$. This specific form of partial wave expansion allows for constraining the parameters that are extracted in the low- t range.

Our simulation program is based upon the constituent quark model approach by Q. Zhao, Z.P. Li, and C. Bennhold [15]; using an effective Lagrangian approach, the interaction between a vector meson and the quarks inside the baryon is described within the $SU(6) \otimes O(3)$ symmetry limit. It further takes into account t -channel exchange mechanisms, which dominate in the low- t range: σ -exchange ($J^\pi = 0^+$) in ρ^0 production and π^0 exchange ($J^\pi = 0^-$) in ω production.

In the s -channel, the helicity amplitudes of all contributing baryons below 2 GeV (cf. $I = \frac{1}{2}$ states in Table 1) are calculated separately, and the excited states at higher masses are treated as degenerate in that scant information is available on these higher baryon resonances. The u -channel contributions include the nucleon and all excited states, with the latter treated as degenerate.

The calculations show that partial widths of those resonances decaying into ωN and the photon helicity amplitudes $A_{\frac{1}{2}}^{\gamma}, A_{\frac{3}{2}}^{\gamma}$ are consistent with the theoretical results of the NRQM approach in Ref. [6]. $P_{13}(1900)$ and $F_{15}(2000)$ have the largest decay widths into ωN ($\sqrt{\Gamma_{\omega}}=1.38$ 1/ $\sqrt{\text{MeV}}$ and 2.64 1/ $\sqrt{\text{MeV}}$) – these results differ from the constituent quark model of S. Capstick and W. Roberts [16] in which the $P_{13}(1900)$ possesses the largest decay width.

Fig. 5 shows the contributions to the differential cross section $\gamma p \rightarrow \omega p$ according to the described model. Major contributions are from pion exchange in the t channel for forward angles (*dashed line*) and resonance formation (*dotted line*). Additionally we plotted the contributions from resonance formation without $F_{15}(1680)$ for $E_{\gamma} \leq 1.4$ GeV and without $F_{15}(2000)$ for $E_{\gamma} > 1.4$ GeV, respectively (*dash-dotted*). The contributions of F_{15} resonances cannot be disentangled from the differential cross section alone as one finds in this figure where the graphs for resonance formation with and without F_{15} contributions overlayed. Predictions on the evolution of the density matrix elements as functions of E_{cm} and θ_{cm} are plotted for a few examples in Fig. 6 and Fig. 7 for the same contributions. These observables are clearly more sensitive on contributions of specific resonances than the differential cross section. Applying the relation of equ. (7) to the calculated density matrix yields the results depicted in Fig. 8. One observes strong fluctuations of the parity asymmetry parameter as a function of the center-of-mass polar angle, which is due to the contributions from the presence of various resonances. The pion-exchange component, however, does not deviate significantly from a parity asymmetry of $P_{\sigma} = -1$. As the observable is plotted in the helicity frame, this statement is true only for $\theta_{cm} = 0, 180^{\circ}$. The variation of P_{σ} with θ_{cm} reflects the kinematical factors that distinguish the Gottfried-Jackson and helicity frames.

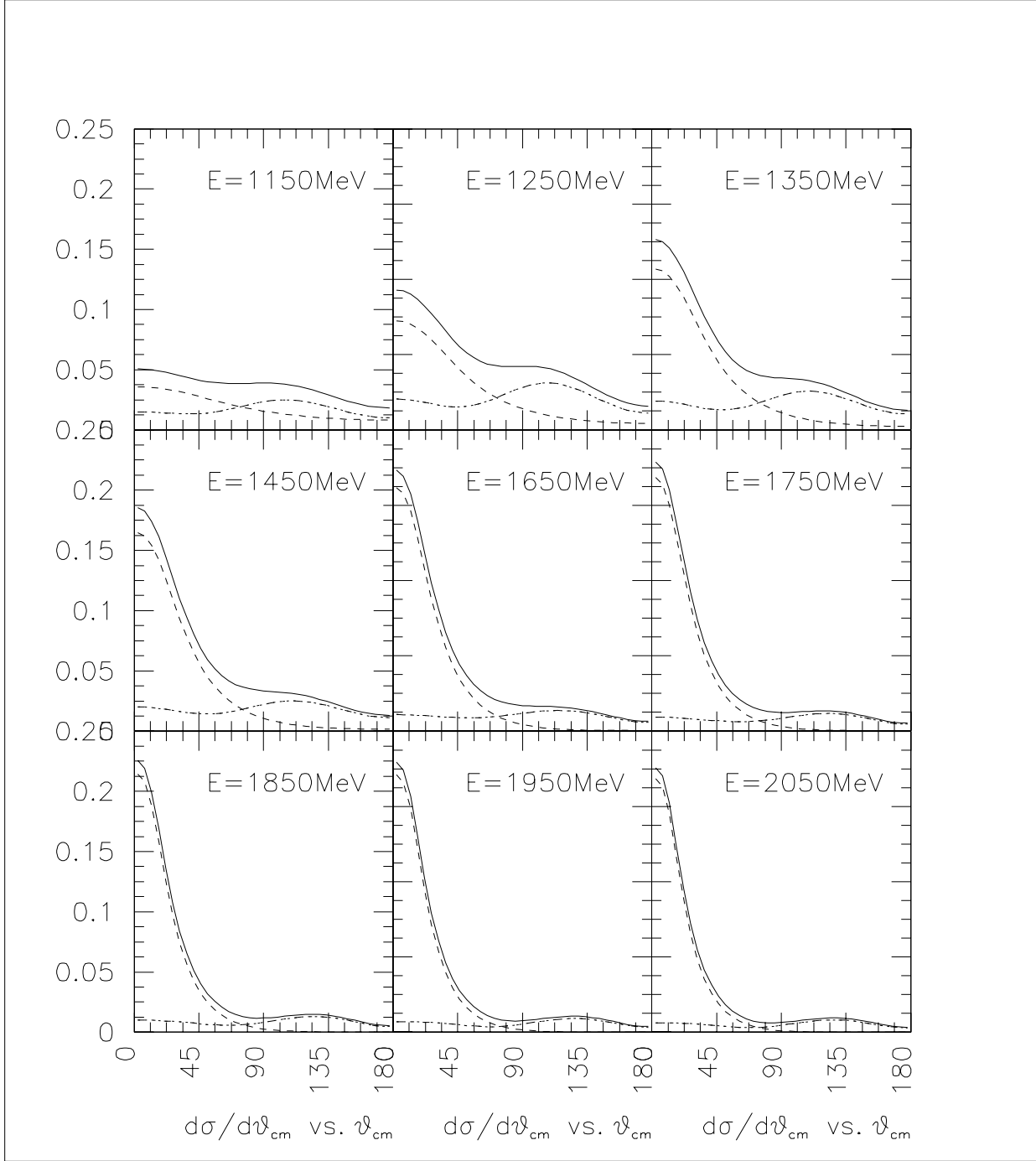


Figure 5: Differential cross section $d\sigma/d\theta_{cm}$ ($\gamma p \rightarrow \omega p$) in the Quark-Model approach of Zhao, Li, and Bennhold. *Solid line*: coherent sum of all contributions, *dashed line*: contribution from pion-exchange, *dotted line*: resonance formation, *dash-dotted line*: resonance formation without $F_{15}(1680)$ for $E_\gamma \leq 1.4$ GeV and $F_{15}(2000)$ for $E_\gamma > 1.4$ GeV.

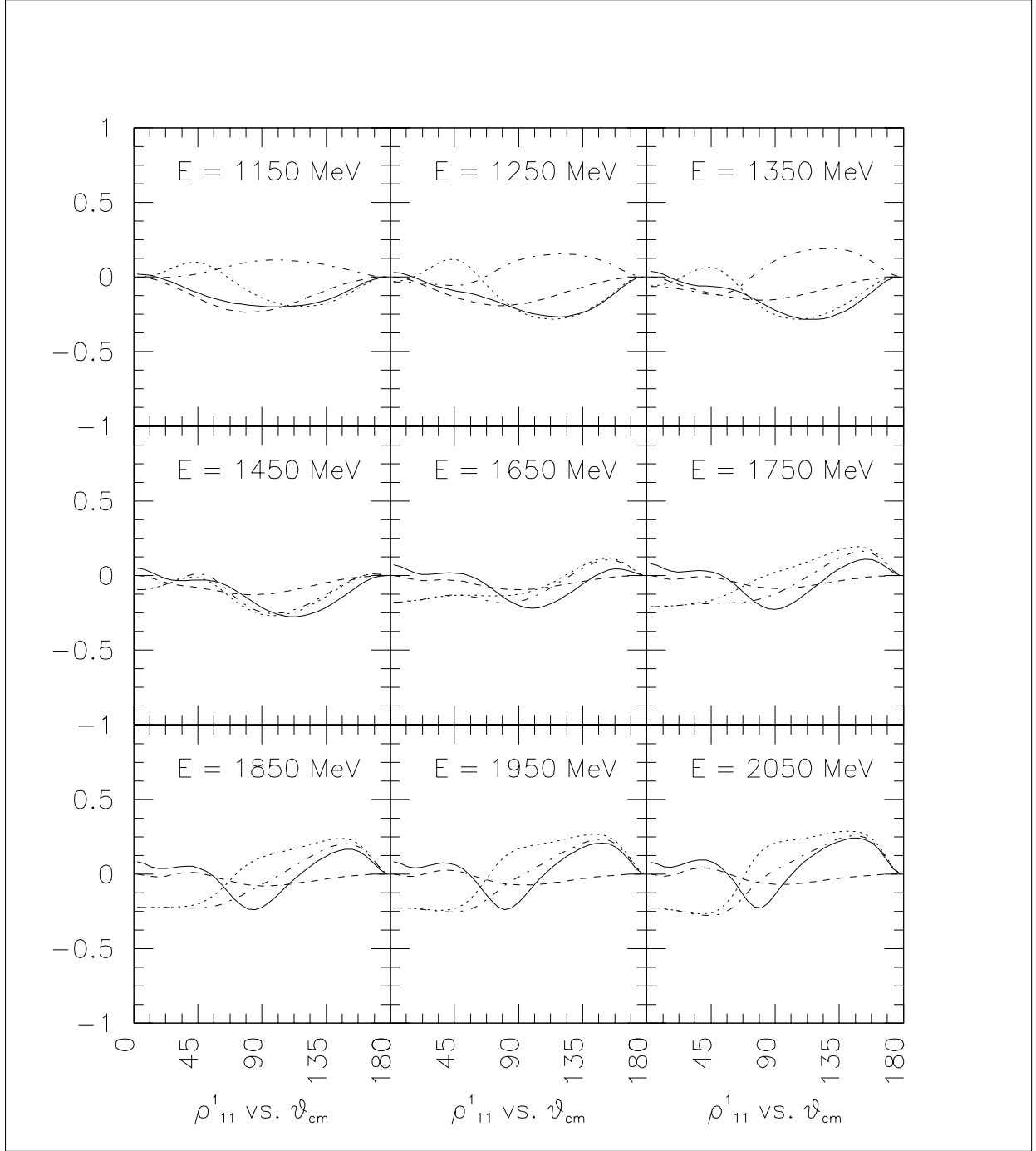


Figure 6: Contributions to the matrix element ρ_{11}^1 in the Quark-Model approach of Zhao, Li, and Bennhold. *Solid line*: coherent sum of all contributions, *dashed line*: contribution from pion-exchange, *dotted line*: resonance formation, *dash-dotted line*: resonance formation without $F_{15}(1680)$ for $E_\gamma \leq 1.4$ GeV and $F_{15}(2000)$ for $E_\gamma > 1.4$ GeV.

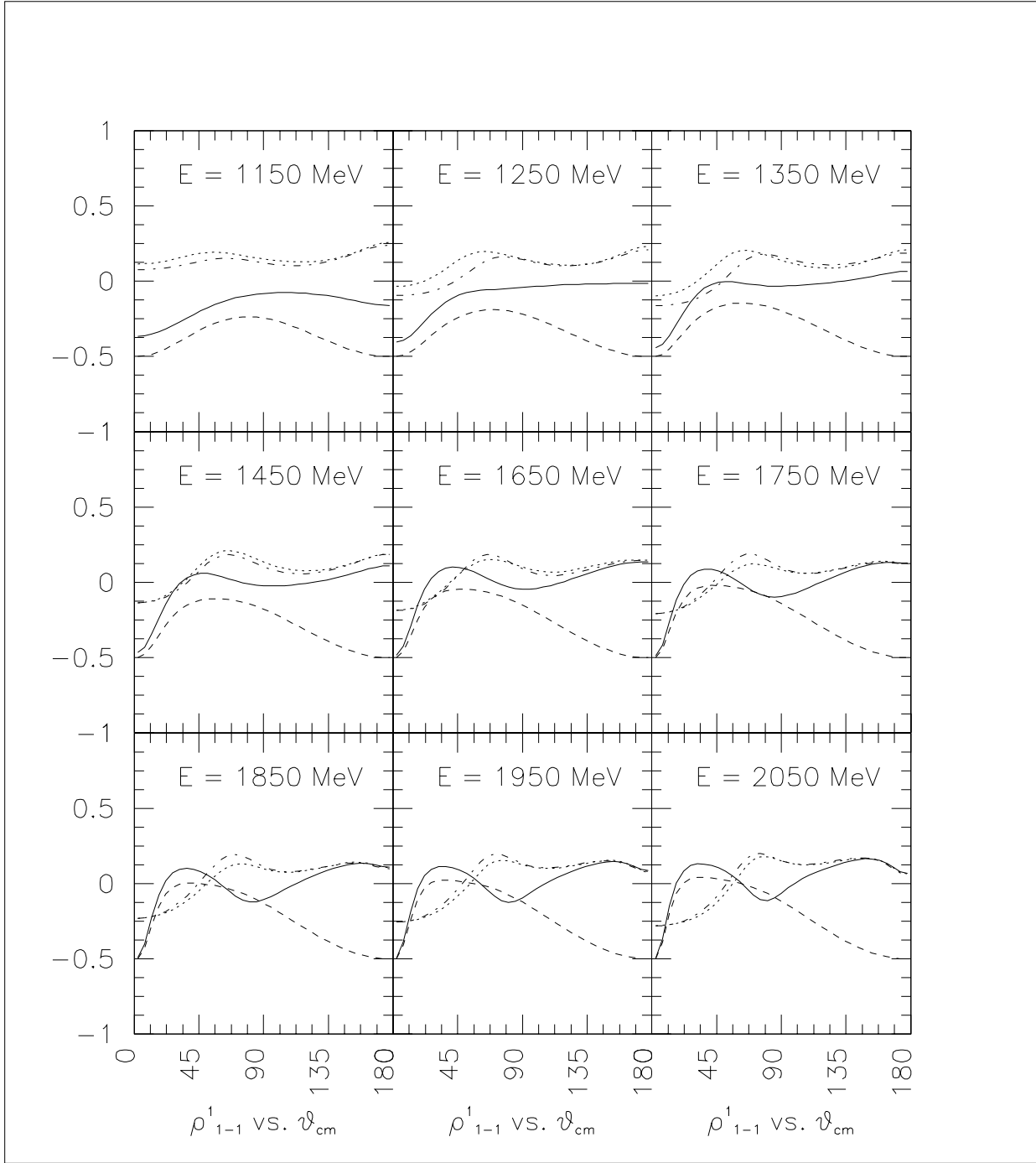


Figure 7: Contributions to the matrix element ρ^1_{1-1} in the Quark-Model approach of Zhao, Li, and Bennhold. *Solid line*: coherent sum of all contributions, *dashed line*: contribution from pion-exchange, *dotted line*: resonance formation, *dash-dotted line*: resonance formation without $F_{15}(1680)$ for $E_\gamma \leq 1.4$ GeV and $F_{15}(2000)$ for $E_\gamma > 1.4$ GeV.

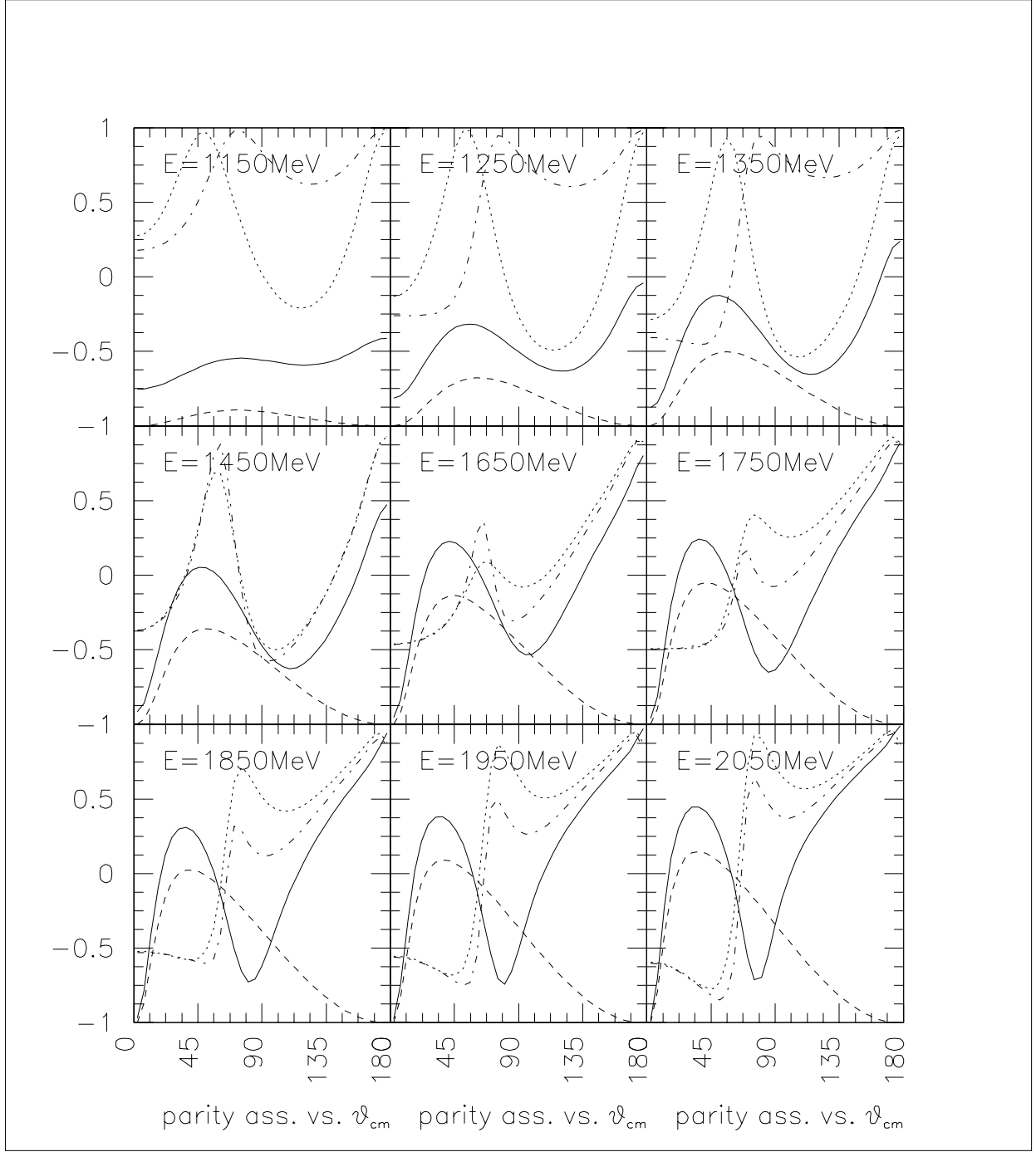


Figure 8: Contributions to the parity asymmetry P_σ in the Quark-Model approach of Zhao, Li, and Bennhold. *Solid line*: coherent sum of all contributions, *dashed line*: contribution from pion-exchange, *dotted line*: resonance formation, *dash-dotted line*: resonance formation without $F_{15}(1680)$ for $E_\gamma \leq 1.4$ GeV and $F_{15}(2000)$ for $E_\gamma > 1.4$ GeV.

3.4 Previous Measurements

Although there have been several experiments on the photoproduction of the ω meson, very few have employed polarized beams, and most of these experiments were performed at photon energies exceeding 3 GeV. The experiments at low energies used bubble-chamber detectors and hence suffered from low statistics [18], [19], [20]. Nevertheless, analyzing the ω decay angular distribution of the SLAC data taken at 2.8, 4.7, and 9.3 GeV, using a linearly polarized photon beam, allowed for the separation of the contributions from natural-parity (i.e. diffractive scattering) and unnatural-parity exchange (i.e. one-pion exchange) [2]. Fig. 9 shows the differential cross section including the contributions of natural parity exchange, and in Fig. 10 the decay angular distributions for all three photon energies are plotted.

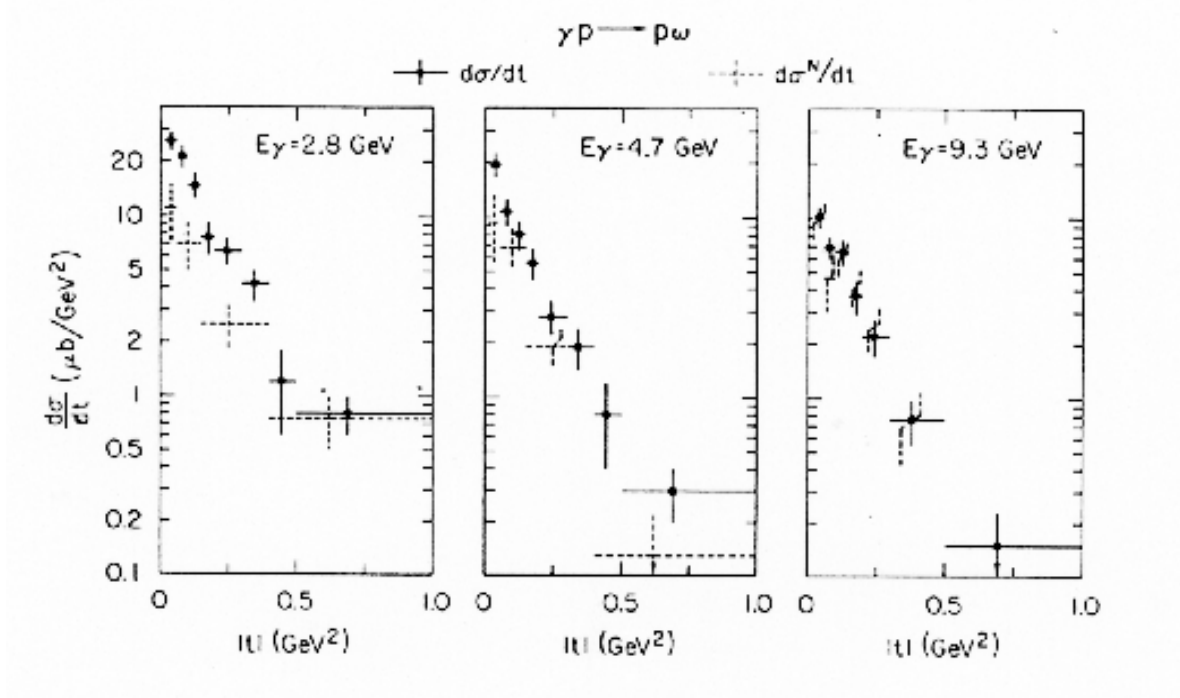


Figure 9: Differential cross section of $\vec{\gamma}p \rightarrow \omega p$ including the contributions from natural-parity exchange (σ^N). The data are from a bubble-chamber experiment at SLAC [2] using monochromatic linearly polarized photons at 2.8, 4.7, and 9.3 GeV.

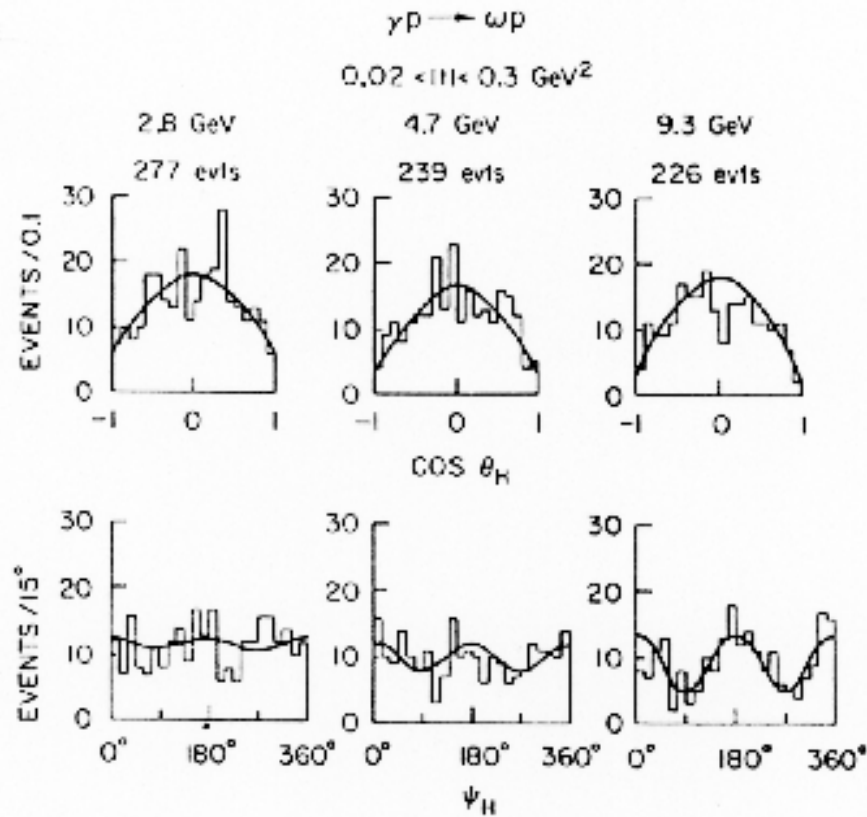


Figure 10: Decay angular distribution in the helicity frame of the same SLAC experiment [2].

We stated in Section 3.2 that the results from the CERN experiment, which collected data on ω photoproduction at much higher photon energies, could be explained purely in terms of VMD, where the reaction proceeds almost entirely through natural-parity exchange in the t channel and is s -channel helicity conserving, as would be expected from diffractive photoproduction [1].

In the photon energy regime near 1.6 GeV ($\sqrt{s} = 1.95$ GeV), however, one would expect to see some indication of resonance production. Unpolarized photoproduction data taken at DESY by [18] are plotted in Fig. 11 (averaging over the photon energy range of $1.4 < E_\gamma < 1.8$ GeV) and compared with the one-pion-exchange model of Friman and Soyeur [4]. The agreement between the data and the curve is good for $|t| < 0.5$ (GeV/c)². In the central region, near $\theta_{cm} = 90^\circ$, the extrapolated curve underpredicts the data by an order of magnitude. The preliminary results from a SAPHIR vector meson photoproduction experiment [21], which used an unpolarized tagged photon beam in the energy range of $1.1 \leq E_\gamma \leq 2.0$ GeV, confirm this observation.

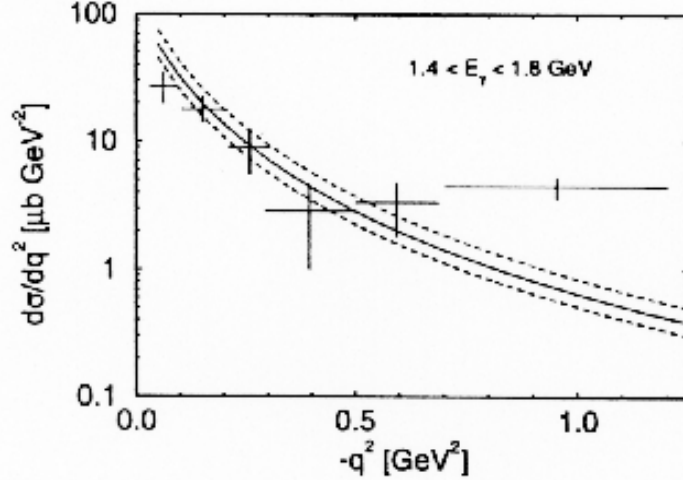


Figure 11: Differential cross section of $\gamma p \rightarrow \omega p$ as measured by the ABBHHM Bubble Chamber Group in comparison to the one-pion-exchange model of Friman and Soyeur.

The differential cross section resulting from SAPHIR is shown in Fig. 12. The curves represent the predictions of purely diffractive (VMD) production ($d\sigma/dt \propto e^{-b|t|}$) and one-pion exchange according to the framework of the Friman and Soyeur model [4]. In the low-energy range ($E_\gamma < 1.35$ GeV), the differential cross section is almost flat with respect to the four-momentum transfer squared. With increasing energy, the exponential falloff with t becomes more pronounced for low t as predicted by pion-exchange and diffractive models. In the mid- t range, however, there are marked departures from the predicted values. It is precisely in this t range where contributions from ω production via s -channel resonances are expected to be most enhanced.

This behavior has been confirmed by the decay angular distribution (in the helicity frame of the ω meson). The angular distributions in Fig. 13 show a more $\cos^2 \theta_{hel}$ -like behavior at lower energies; at higher photon energy ($E_\gamma > 1.8$ GeV), however, the decay angular distribution becomes more diffractionlike. In case of s -channel helicity conservation (SCHC) the angular distribution is expected to be proportional to $\sin^2 \theta_{hel}$, and flat in ϕ_{hel} . The distributions shown in Fig. 13 (*bottom*) at c.m. energies around 1.85 to 1.95 GeV, in the mid- t range, reflect a \cos^2 -like behavior of the decay polar angle θ_{hel} , indicating contributions from spinflip amplitudes; departures from a flat ϕ_{hel} distribution signal the presence of nonzero matrix elements $\rho_{11}^0, \text{Re}\rho_{10}^0$, and further indicate interferences in the

spinflip and non-spinflip amplitudes.

By extrapolating to $t = 0$ and integrating over the full t range, one can obtain the total cross section (cf. Fig. 14). The steep increase at the ω photoproduction threshold ($E_\gamma = 1.1$ GeV) cannot be explained within the framework of the model of Friman and Soyeur or from vector meson dominance alone. The almost flat differential cross section near threshold and the non-SCHC decay angular distribution in this energy range as well as the steep increase of the total cross section from threshold strongly hint towards the presence of underlying baryon resonances. Such a resonance at $\sqrt{s} \sim 1.78$ GeV has been observed in the reaction $\pi^+ p \rightarrow \pi^+ \pi^+ \pi^- \pi^0 p$ [22].

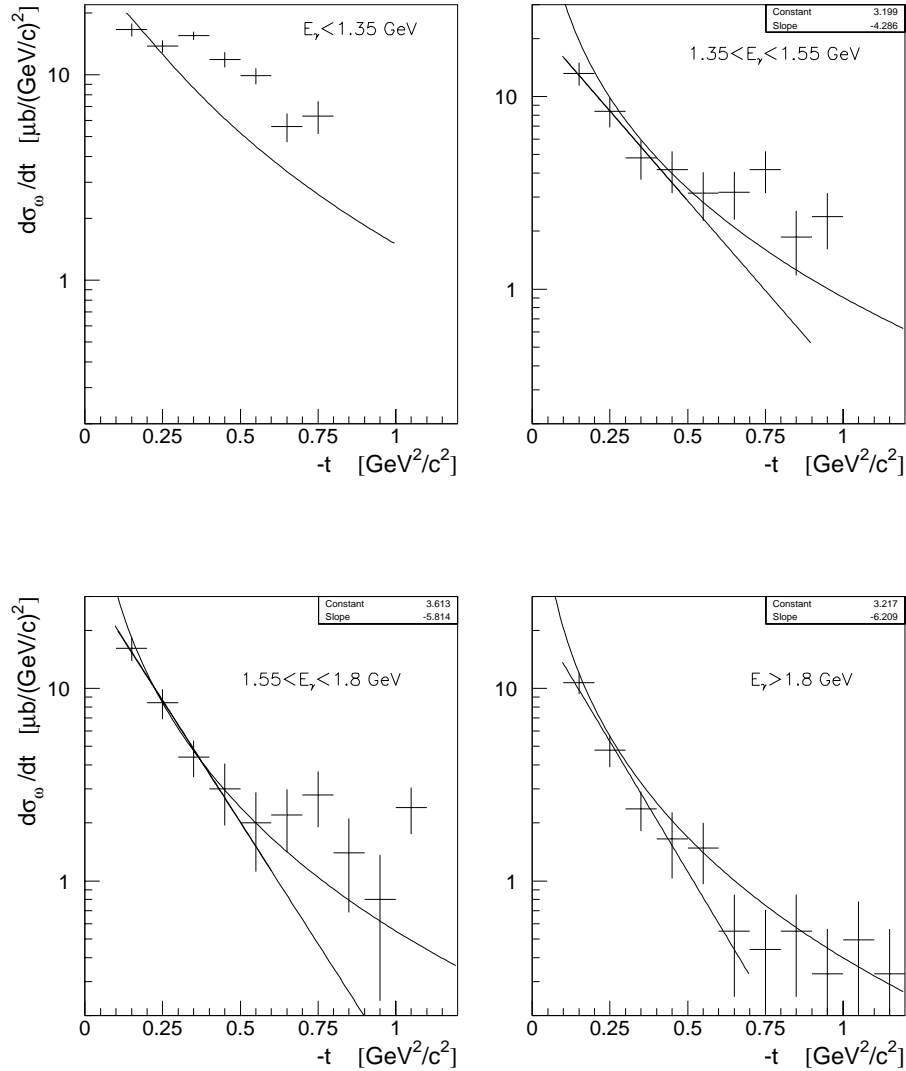


Figure 12: Differential cross section $\gamma p \rightarrow \omega p \rightarrow \pi^+ \pi^- \pi^0 p$. SAPHIR data in comparison with predictions of the model of Friman and Soyeur (*curve*) and exponential fit to SAPHIR data (*exponential line*).

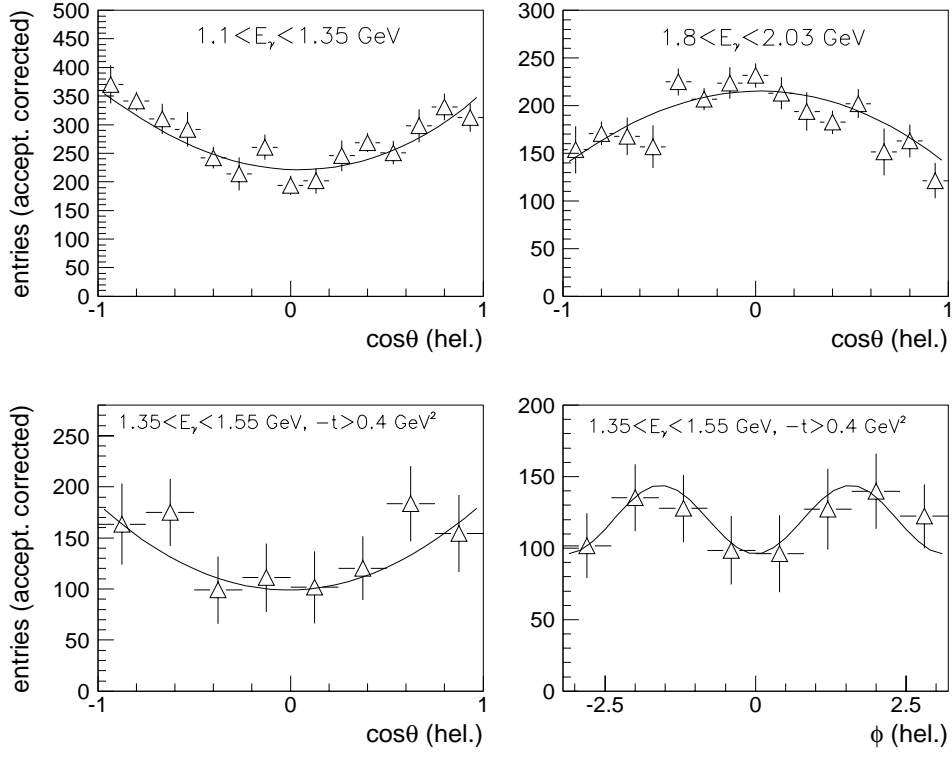


Figure 13: Decay distribution of ω in selected ranges of E_γ and t . The curves correspond to fits to the decay angular distribution $W^0(\cos \theta_{hel}, \phi_{hel})$ as is defined in equ. (2).

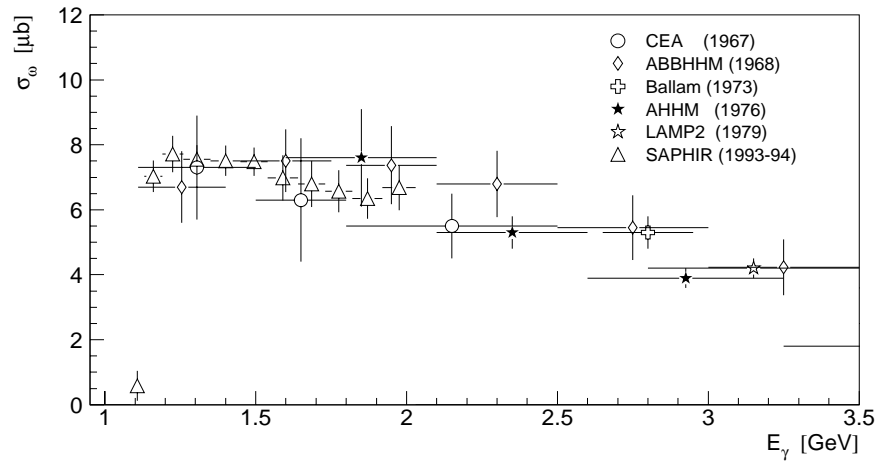


Figure 14: Total cross section for $\gamma p \rightarrow \omega p \rightarrow \pi^+ \pi^- \pi^0 p$ at low photon energies.

4 Acceptance Studies

In this section we first discuss our acceptance studies for the ω channel. We will then show the results of these ω -extraction techniques that we have applied to the **g1** photoproduction data set; these data were collected in the summer of 1998.

4.1 Identification of the Omega Meson Signal

Here we report our acceptance studies, summarizing the main results and the techniques that we have developed in distinguishing the reaction $\gamma p \rightarrow p\omega$ from either the two-pion or three-pion backgrounds.

The event generators are based upon those described in [21], [24], and [23]. They were used to realistically distribute the ω signal and three-pion background events. Using the simulation program mentioned in Section 3.2, we studied the decay angular distributions with regard to the sensitivity for variations of the spin density matrices. We made use of the simulation package FASTMC_GEN [25], which renders a reasonably realistic representation of the geometry and mass distribution of the conceptual design of the CLAS detector including detector efficiencies. We also employed the CLAS simulation and reconstruction program SDA [26]. We incorporated track finding and fitting algorithms which require track elements in only two of the three drift chambers. After distributing the decay products from our ω event generator and processing the events through the simulation programs, we then extracted the density matrix elements by means of a maximum-likelihood fit using the CERN package MINUIT [27].

The primary difficulty in identifying the photoproduced ωp channel is in efficiently separating ω -meson from non- ω -meson events without unduly sacrificing the acceptance. In a first approach, the events were generated uniformly in phase space. The daughter pions created from the decay of the parent vector meson, too, were uniformly distributed in the phase space of the rest frame of the omega meson. The final-state particles were then Lorentz boosted to the laboratory frame, and subsequently were fed into the CLAS simulation program FASTMC_GEN. We initially generated 50,000 ωp events and background ($p\pi^+\pi^-\pi^0, p\pi^+\pi^-$) studies at thirteen different incident photon energies between $E_\gamma=1.125$ and 2.2 GeV, and two field settings for the CLAS torus magnet, $B/B_o = +0.5$ and $+1.0$. We

found that the cuts effectively eliminated $\pi\pi$ background events. We have focused on the $\omega \rightarrow \pi^+\pi^-\pi^0$ decay mode, requiring that we identify the two positively charged final-state particles, π^+ and proton, and thereby obtain the complete four-momentum information. Both the proton and the π^+ must have registered hits in all three drift chambers and have deposited energy in a ToF scintillator. On the other hand, we require that the π^- have hits in the inner **two** drift chambers. From this selection criterion, we only obtain momentum and charge information but cannot identify the particle. We associate this track to a π^- and thereby obtain its energy from the relationship $E^2 = p^2 + m_{\pi^-}^2$. We now have the complete four-momentum of the three charged final-state particles and the energy of the incident photon, which we have smeared with a uniform ΔE_γ of $\pm 0.1\%$ consistent with the resolution of the bremsstrahlung tagger. From the calculated missing mass of the simulated events, we identify a π^0 as that particle with a mass in the range of $0.09 \leq m_x \leq 0.20$ GeV/c². This cut effectively eliminates two-pion channel events, i.e. $\gamma p \rightarrow p\rho^0$, $\gamma p \rightarrow \Delta\pi$, or $\gamma p \rightarrow (p\pi^+\pi^-)_{\text{p.s.}}$. In Fig. 15 we plot the reconstructed mass of the π^0 for various incident photon energies for the omega signal channel $p(\gamma, p\pi^+\pi^-)\pi^0$. Clearly, this π^0 cut by itself cannot eliminate the $p\pi^+\pi^-\pi^0$ background events.

π^0 mass from $p(\gamma, p\pi^+\pi^-)\pi^0$

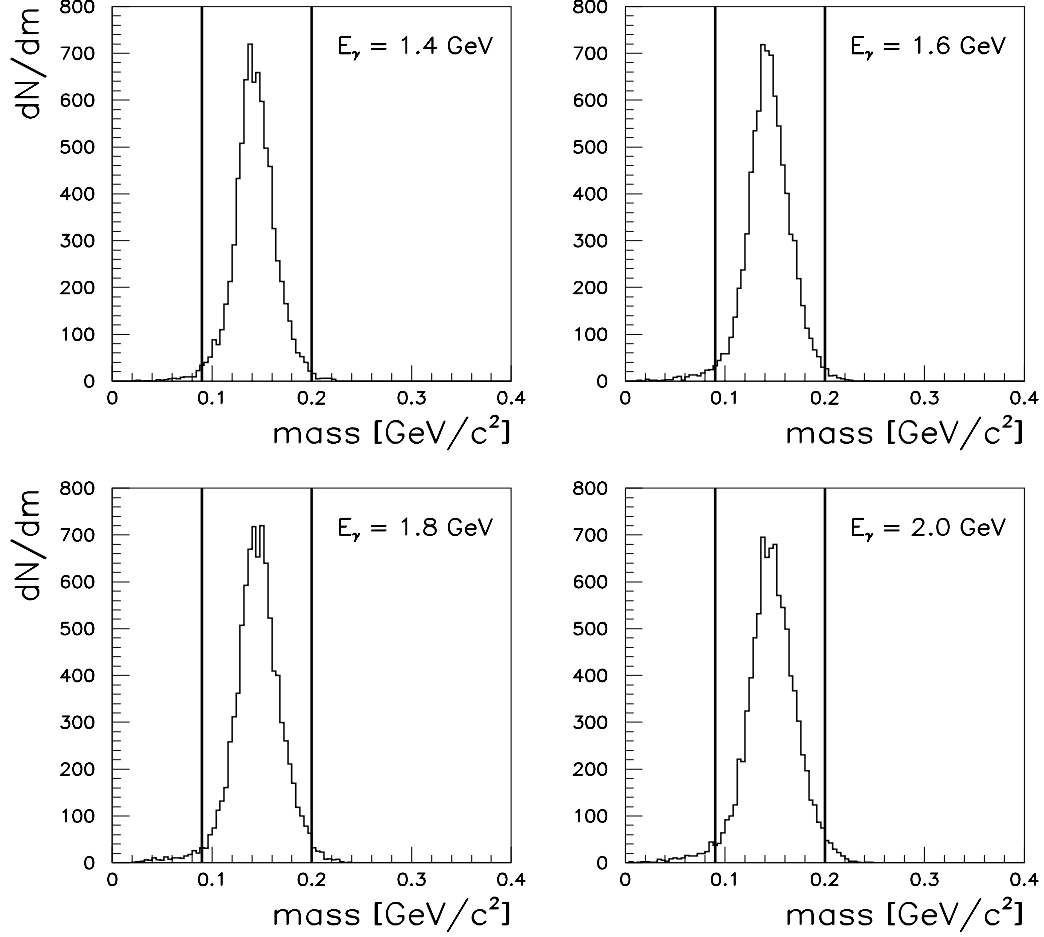


Figure 15: The missing mass distributions for various incident photon energies are plotted for $B/B_o = +0.50$. The missing mass is obtained from the smeared tagged photon, the particle-identified proton and π^+ , and the momentum-determined π^- . Those events with masses in the range of $0.09 \leq m_x \leq 0.20$ GeV/c² are considered to have a π^0 in the final state.

Because the mass peak of the ω meson is so sharp, a cut on the invariant mass of the three final-state pions alone will serve to extract this vector meson signal if the $\pi^+\pi^-\pi^0$ background is minimal. In Fig. 16, we show the raw acceptance of the phase space distributed signal and background events. For the mid- t kinematic regime, where the signal for s -channel resonances are most pronounced, we presume the N^* differential cross section is flat. Only for low t does one observe an exponential falloff in the differential cross section for the VMD-produced omega mesons. We have also distributed the background $\pi^+\pi^-\pi^0$ events uniformly in phase space. We see in Fig. 16 that the acceptance for background events in the three-pion invariant mass range $0.75 \leq m_{\pi^+\pi^-\pi^0} \leq 0.81$ GeV decreases with increasing photon energy due to the fact that the phase space covers a larger kinematical range at higher energies.

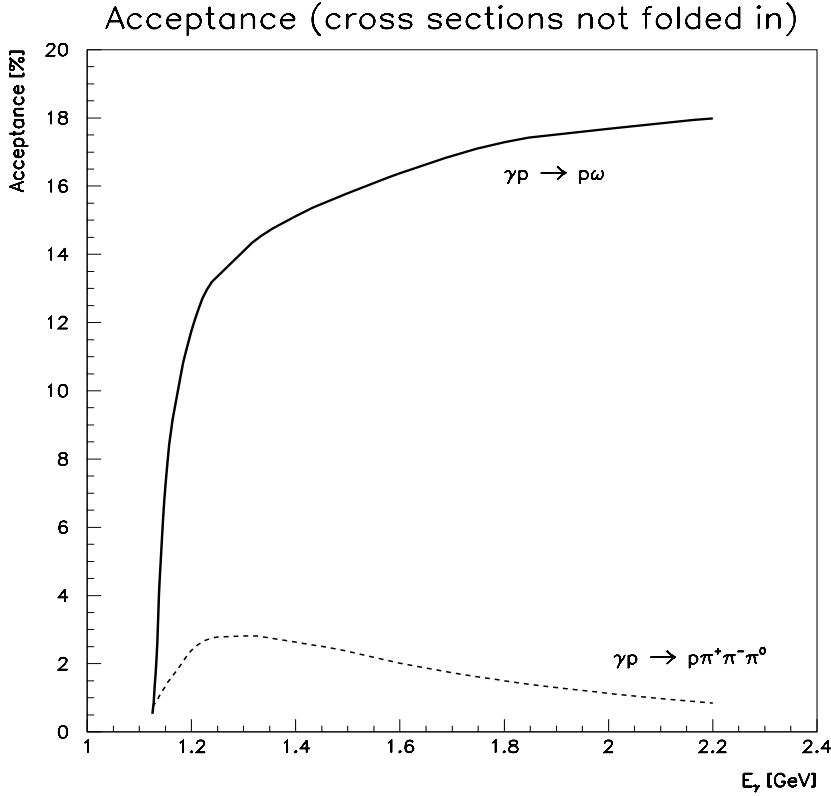


Figure 16: The overall acceptance is plotted as a function of the incident photon energy for $B = +0.50B_0$ for (solid line) $\gamma p \rightarrow p\omega$ and (dashed line) $\gamma p \rightarrow p\pi^+\pi^-\pi^0$. Only a simple invariant-mass cut of $0.75 \leq m_{\pi^+\pi^-\pi^0} \leq 0.81$ GeV was employed to identify the omega meson.

In Fig. 17 we plot the acceptance for the reaction $\gamma p \rightarrow \omega p$ as a function of the ω production angle θ_{cm} for selected photon energies. In general — and especially in the mid- t regime — the acceptance for this reaction is much larger than when all three charged particles are identified as described above (*solid line*); only in forward direction at higher energies the acceptance is higher when we require both positively charged particles and both photons of the π^0 decay to be detected (*dashed line*).

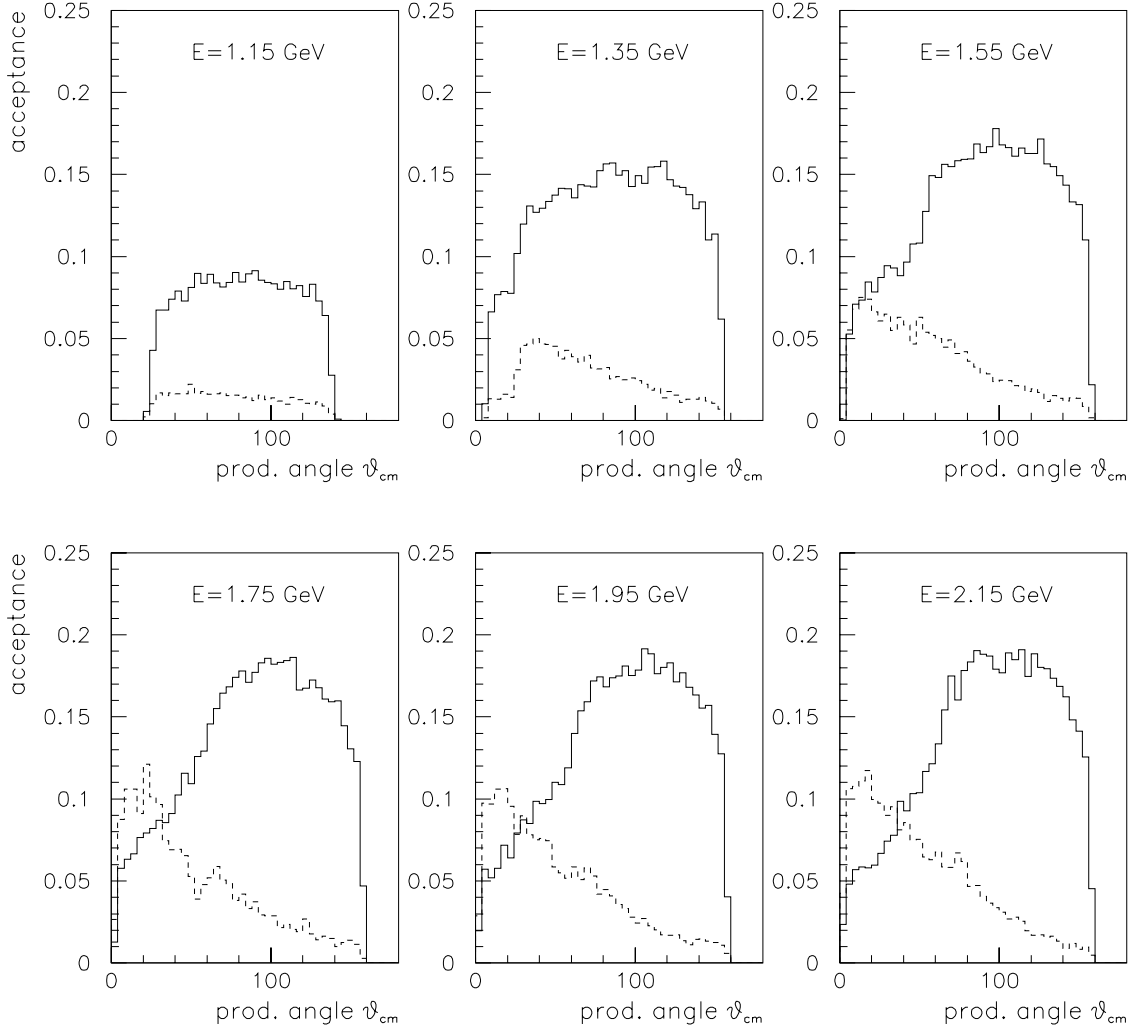


Figure 17: Acceptance for $\gamma p \rightarrow \omega p$ as a function of the production angle θ_{cm} for the two methods to identify the process as described in the text above.

The ω signal itself is extracted in the three-pion effective mass distribution by fitting to the background. We have studied the effects of varying the ratio of the ω signal to the $\pi^+\pi^-\pi^0$ background as a function of incident photon energy. We generated 100,000 of these combined phase-space distributed signal and background events for $|t| > 0.3 \text{ (GeV/c)}^2$, and processed them through FASTMC_GEN. We plot some of the results in Figs. 18 and 19. In this mid- t range, one sees that the omega peak remains prominent even for $E_\gamma = 1.2 \text{ GeV}$ with the signal being only 5% of the total cross section. We fit the background with a polynomial function. From this fit, we can extract the omega signal from the three-pion background on a bin-by-bin basis. We then fit this extracted signal with a gaussian, and find that the centroid and the width of the peak is consistent with the expected values of the omega meson, with the CLAS detector smearing folded in, as is shown in Figs. 20 and 21.

In summary, the omega channel is exceptionally clean. We have found that our acceptances are quite flat as a function of magnetic field strength above $B = +0.50B_0$.

invariant mass of ω signal and $\pi^+\pi^-\pi^0$ background

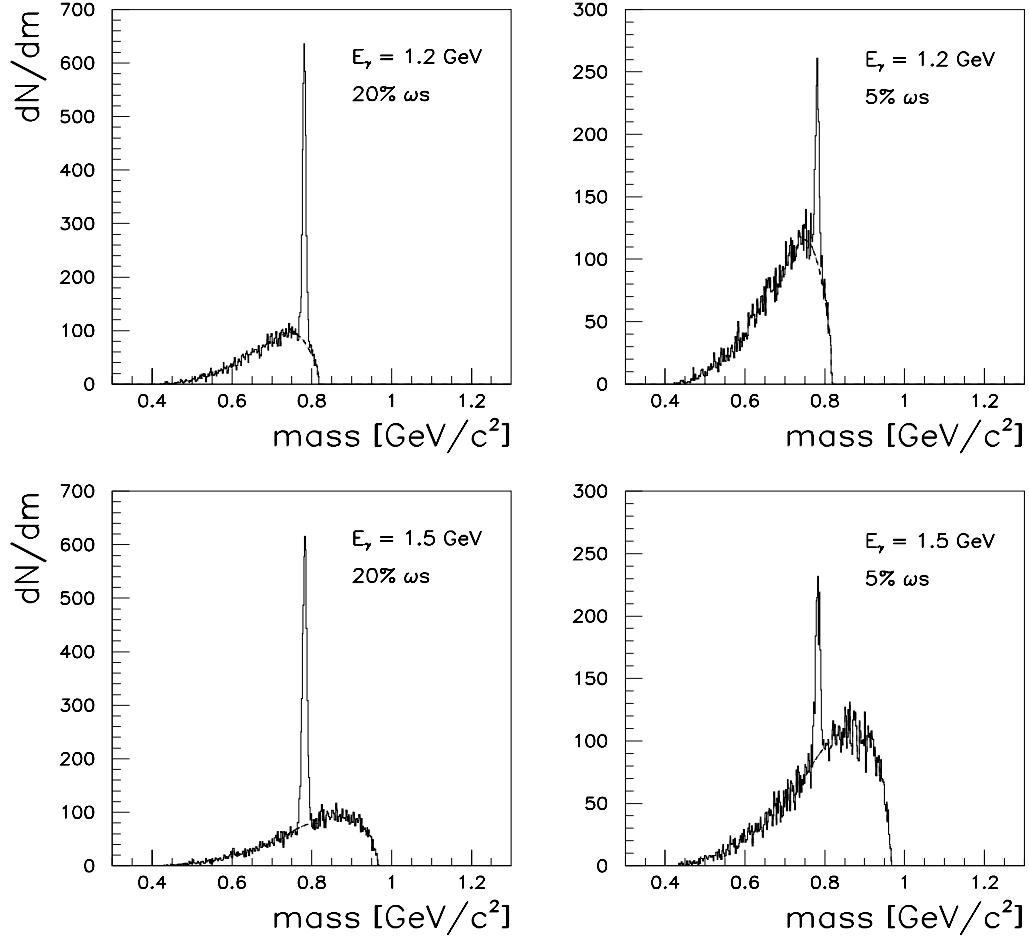


Figure 18: The invariant mass of the ω -signal, superimposed upon the $\pi^+\pi^-\pi^0$ -background events, is plotted for two incident photon energies and two signal-to-background ratios. The background is fit with a polynomial function.

invariant mass of ω signal and $\pi^+\pi^-\pi^0$ background

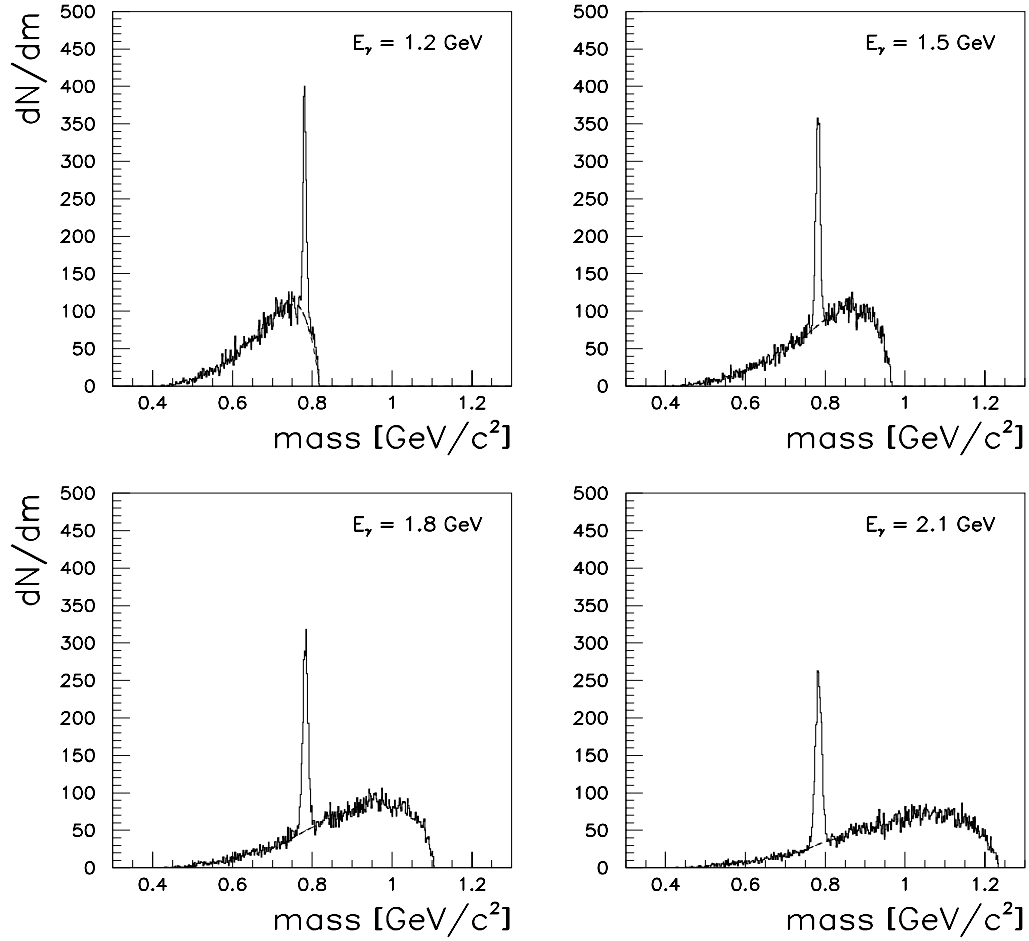


Figure 19: The invariant mass of the ω -signal, superimposed upon the $\pi^+\pi^-\pi^0$ -background events, is plotted for four different incident photon energies with a fixed signal-to-background ratio of 10%. The background is fit with a polynomial function.

invariant mass of ω signal with $\pi^+\pi^-\pi^0$ background subtraction

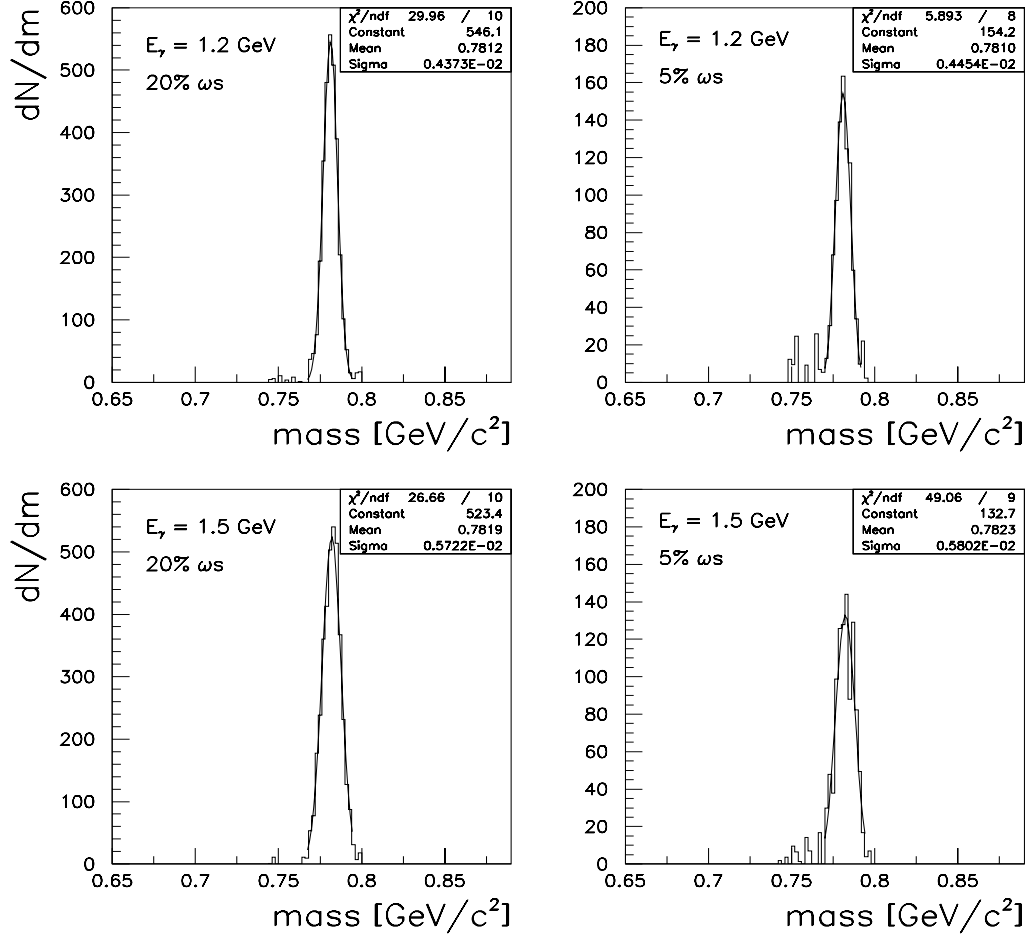


Figure 20: The extracted ω signal for two incident photon energies and two signal-to-background ratios. A gaussian is fit to the extracted ω signal.

invariant mass of ω signal with $\pi^+\pi^-\pi^0$ background subtraction

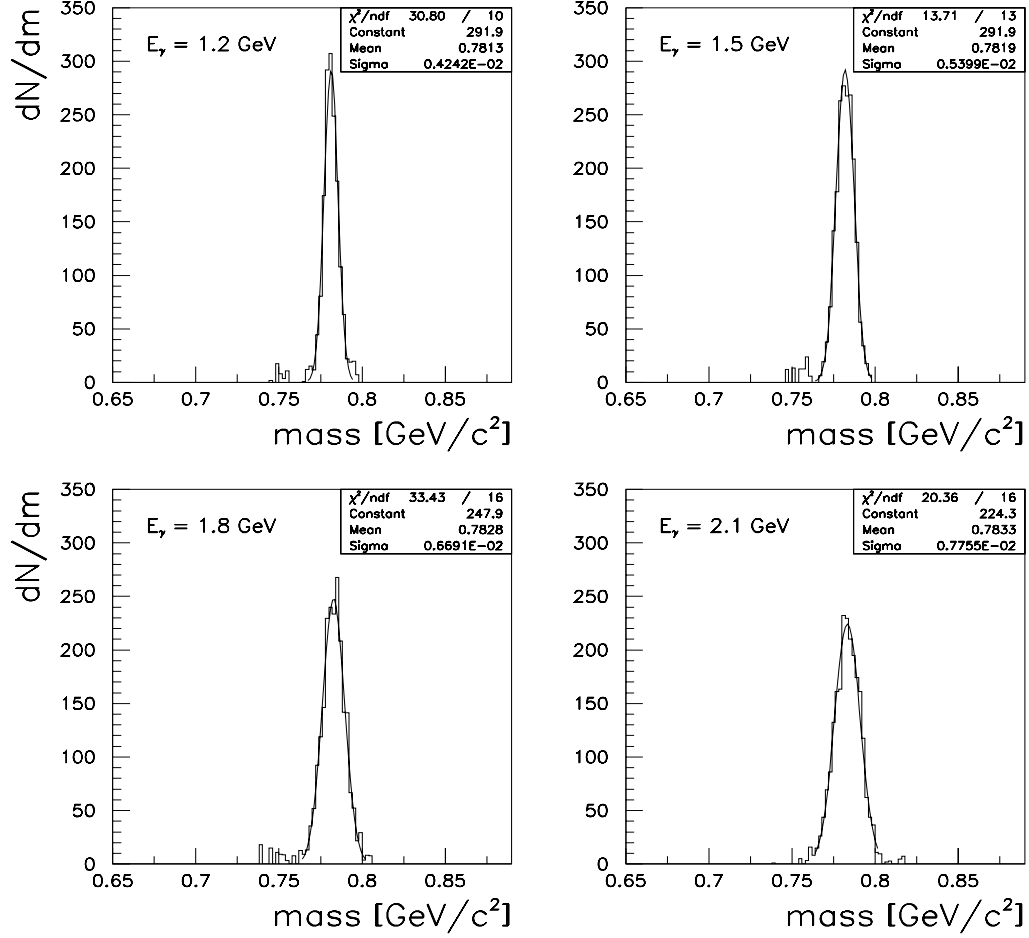


Figure 21: The extracted ω signal for four incident photon energies and a fixed signal-to-background ratio of 10%. A gaussian is fit to the extract ω signal.

4.2 First analysis of ω photoproduction data at CLAS

We have begun analyzing the g1 photoproduction data taken in June '98, where we have applied the aforementioned ω -selection criteria. Despite the preliminary state of both the detector calibrations and the acceptance/efficiency studies, we can extract the ω signal quite well. Fig. 23 shows some preliminary results for the W range between 1.9 and 2.1 GeV obtained from the analysis of about 7% of the data set.²

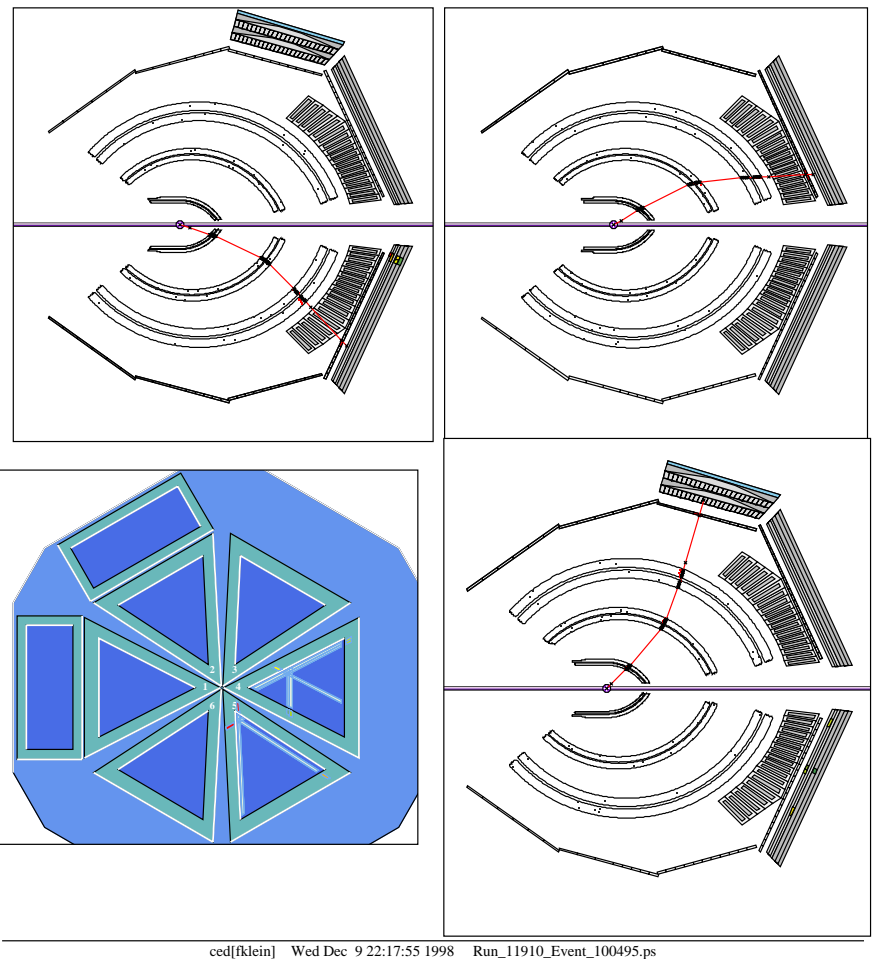


Figure 22: Completely detected $p\pi^+\pi^-\pi^0$ event from the g1 photoproduction data run.

²Here we only show mass distributions. As soon as the normalization and efficiency questions are settled, preliminary cross section data can be presented.

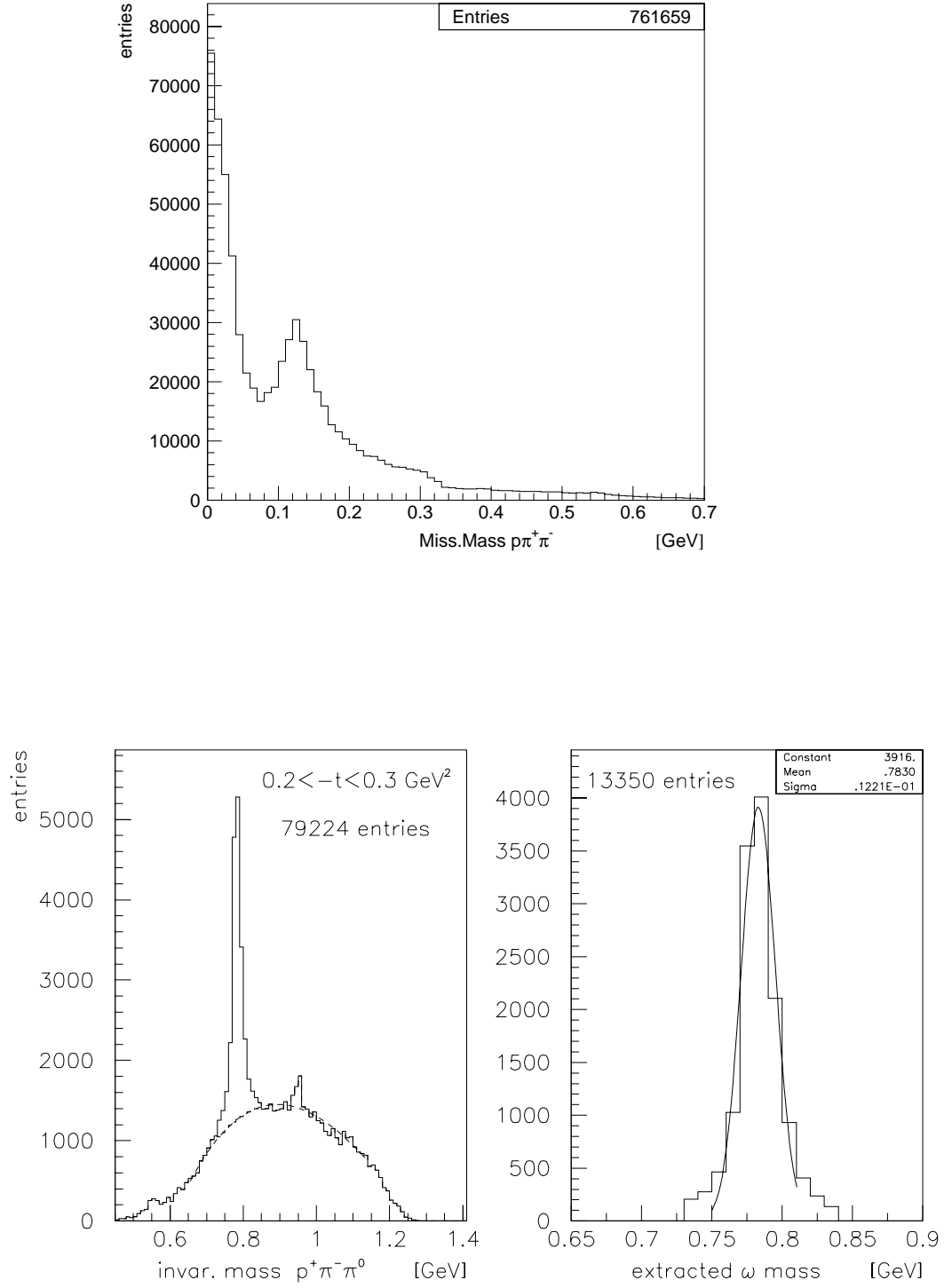


Figure 23: Missing mass distribution for the reconstructed $p\pi^+\pi^-$ (top) and extraction of the ω signal (bottom) in the W range between 1.9 and 2.1 GeV (subset of g1 data at $E_0 = 2.487$ GeV).

We shall also analyze the triple-pion data taken during the second part of **g1** (August '98). In fact, one of the cospokespersons of this proposed experiment has assigned his graduate student to pursue these studies for his Ph.D. thesis topic. This data set was produced with circularly polarized photons on hydrogen. The polarization is given approximately by

$$P_{circ} = P_{el}(4x - x^2)/(4 - 4x + 3x^2) \quad \text{with } x = k_\gamma/E_{el}.$$

With an obtained electron polarization of 67%, the photon circular polarization is about 67% at the bremsstrahlung endpoint and about 36% at $k_\gamma/E_{el} = 0.5$. Extracting the ω decay angular distributions for these data sets, $W^0(\cos\theta, \phi)$ and $W^3(\cos\theta, \phi)$, provide additional constraints for our final analysis.

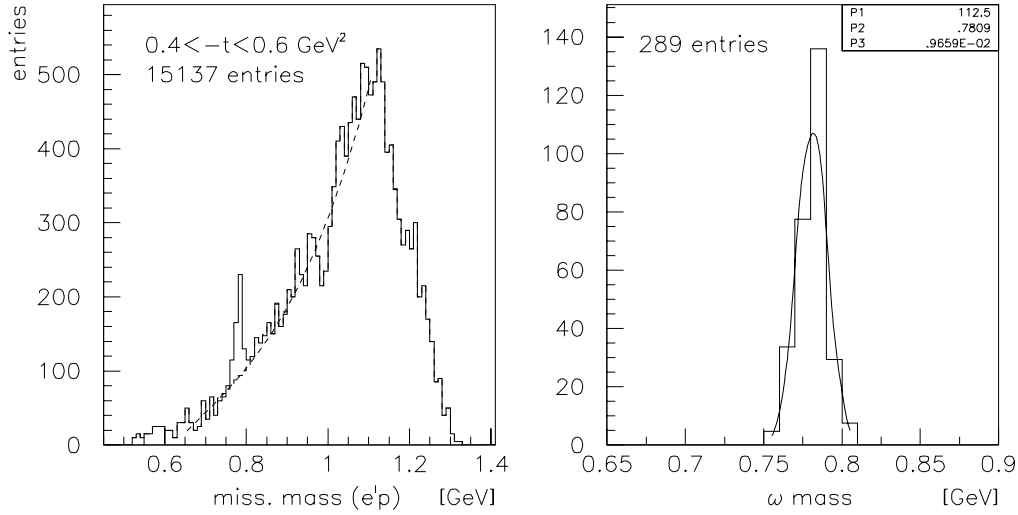


Figure 24: Extraction of the ω if only one proton, a π^+ and one photon are identified (**e1** data at $E_0 = 4.045$ GeV for $W=2.1$ to 2.3 GeV, $Q^2=1.0$ to 1.5 GeV 2).

The ω channel can as well be identified by detecting both positively charged particles (p, π^+), together with one of the photons from the π^0 decay. Even though the background is much larger, the ω meson signal can clearly be identified as is shown in Fig. 24 where semi-inclusive data $p(e, e'p\pi^+\gamma)X$ of the **e1** run period for specific W and Q^2 ranges are shown. The ω peak towers over the background in the missing mass distribution $MM(p(e, e'p)X)$. However, in order to extract the decay angular distribution, and thereby the density matrix elements, it is not sufficient to identify one of the charged pions together with one of the

photons from the π^0 decay: one has to identify at least two pions of the ω decay.³

4.3 Extraction of the Density Matrix Elements

Employing our simulation programs, we distributed the generated events of the $\gamma p \rightarrow \omega p$ reaction in accordance with the angular distributions, which we calculated for various production processes. The polarization vector of the incident photon was held constant. For the case when all three final-state charged particles were accepted, we cut on the missing π^0 mass and plotted the effective three-pion mass distribution versus the decay angles θ_{hel} and ϕ_{hel} in the helicity frame. We identified the ω by fitting on the mass distribution $M_{\pi\pi\pi}$ within each bin of θ_{hel} and ϕ_{hel} . The nine coefficients of the density matrices are then extracted via a maximum-likelihood fit, similar to the approach used in our approved experiment [24], where we extracted the density matrix elements for the decay kaons in ϕ -meson photoproduction.

As an example the results for one of the matrix elements and the parity asymmetry which is calculated via equ. (7) are shown in Fig. 25. We generated the events assuming one-pion exchange as production process.

³As shown in Fig. 2, the decay angles θ, ϕ are defined with respect to the normal to the decay plane.

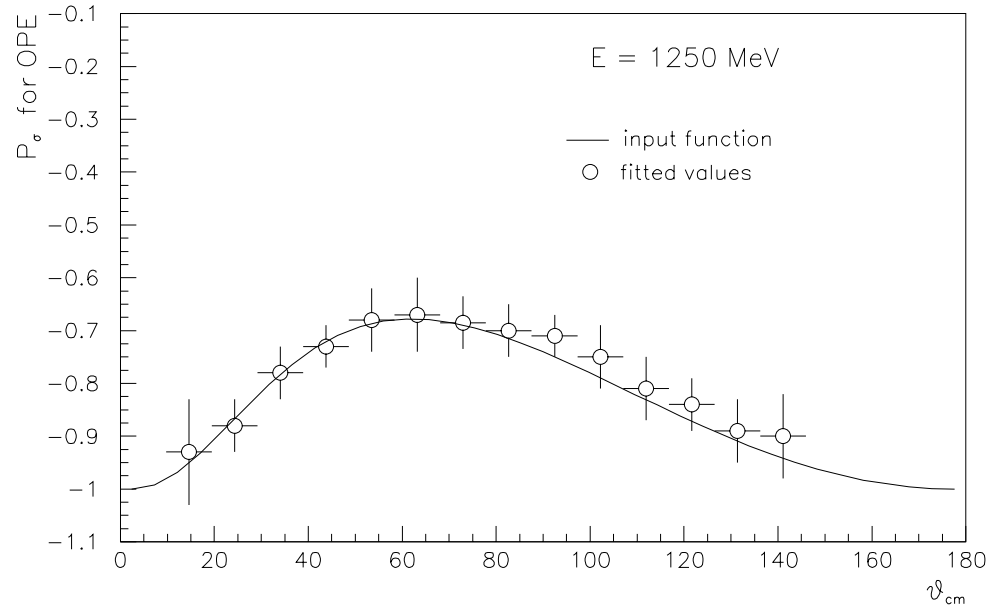
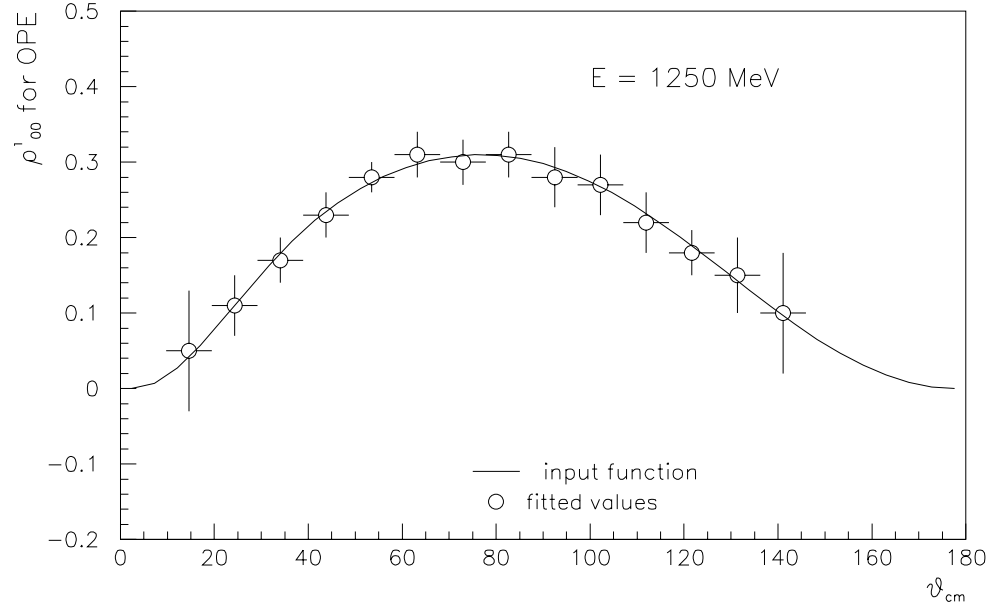


Figure 25: Extracted density matrix element and parity asymmetry (*open circles*) for generated one-pion exchange process (generated values: *curves*).

5 Experimental Parameters

5.1 Linearly Polarized Photons

We propose to use a linearly polarized beam of photons produced from the recently approved Coherent Bremsstrahlung Facility. This technique of obtaining linearly polarized photons has successfully been employed at both SLAC [29] and Mainz [30]. Detailed discussions of the underlying theory of coherent bremsstrahlung can be found in references [31], [32], [33], and [34].

The spectrum of a photon beam produced coherently from a crystal radiator has several distinguishing characteristics compared with that of incoherent bremsstrahlung. The salient features of coherent bremsstrahlung are:

1. An energy spectrum with discrete peaks due to the varying contributions of different reciprocal lattice vectors
2. A strong linear polarization within each of the peaks
3. A polar angle distribution which is correlated with the energy of the photon
4. Tunable peak energies by crystal choice and orientation
5. The direction of the polarization can be quickly and smoothly changed by rotating the crystal radiator

We shall discuss each of these above points in turn.

For an electron of energy E_o to radiate a photon of energy k requires that momentum \vec{q} be transferred to a nucleus in the crystal lattice. The allowable range of momenta transfers are confined to the volume of a *pancakelike* region in momentum space, where the pancake conditions are given by

$$\delta \leq q_\ell \leq 2\delta \tag{13}$$

$$0 \leq q_\perp \leq 2x \tag{14}$$

where x is the fractional photon energy, k/E_o , and

$$\delta = q_\ell^{\min} = \frac{1}{2E_o} \frac{x}{1-x}. \tag{15}$$

We will use the natural units ($\hbar = c = m_e = 1$) unless specifically marked otherwise. The influence of the crystal structure is given by the Laue condition

$$\vec{q} = \vec{g}. \quad (16)$$

Here \vec{g} is the reciprocal lattice vector. Several reciprocal lattice vectors can contribute simultaneously if the orientation of the crystal with respect to the direction of the incident electron beam is not carefully selected. This leads to overlapping peaks which will smear out the direction of the polarization. For the following discussion we will assume we have selected the well isolated reciprocal lattice vector with the Miller indices of $(02\bar{2})$, which gives $|\vec{g}| = \frac{2\pi}{a}\sqrt{2^2 + 2^2}$, and where a is the length of the fundamental cell. For the case of diamond, $a = 925$ in dimensionless units. The corresponding momentum transfer to the lattice nucleus is then $|\vec{q}| = 9.85 \text{ keV}/c$ for $(02\bar{2})$. Selecting a specific q_ℓ in the range between δ and 2δ with respect to the electron momentum produces coherent-bremsstrahlung photons of the corresponding fractional energy x . Maximum linear polarization is found in the plane defined by the reciprocal lattice vector and the 3-momentum of the incident electron, i.e. (\vec{g}, \vec{p}_o) .

The angular distribution of the coherent and incoherent bremsstrahlung photons are very different. Whereas the polar angular distribution of the incoherent bremsstrahlung photons is *independent* of the photon energy

$$\frac{dN(\theta)}{d\theta} = \frac{\theta}{(1 + \theta^2)^2}, \quad (17)$$

the emission angle of the coherent bremsstrahlung photons *decreases* with increasing photon energy ($x \leq x_d$)

$$\theta^2 = \frac{1-x}{x} 2E_o q_\ell - 1 = \frac{1-x}{x} \cdot \frac{x_d}{1-x_d} - 1. \quad (18)$$

Here x_d is the maximum fractional photon energy for a given setting of the crystal

$$x_d = \frac{2E_o q_\ell}{1 + 2E_o q_\ell}, \quad (19)$$

and the θ s are given in units of characteristic angle, i.e.

$$\theta_{\text{char}} = \frac{m_e c^2}{E_o}. \quad (20)$$

For example, for $E_o = 4.0 \text{ GeV}$, $\theta_{\text{char}} \simeq 1/8 \text{ mrad}$.

We have developed a Monte Carlo which samples the probability density bremsstrahlung spectrum as a function of fractional energy x , and polar angle θ . The incoherent and coherent

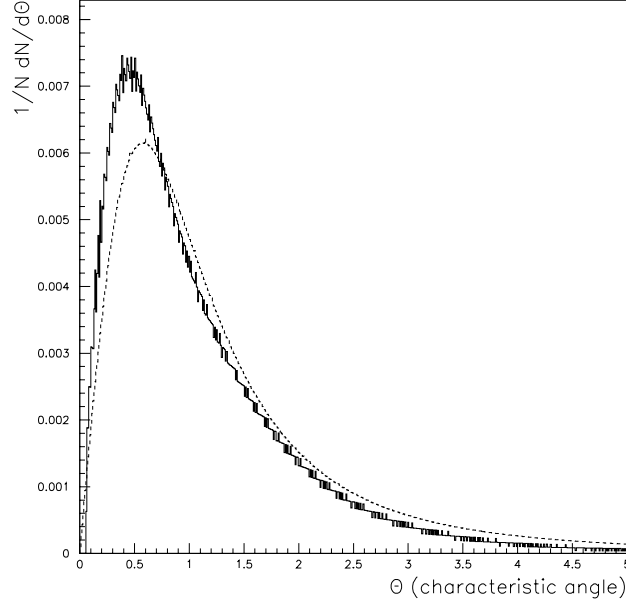


Figure 26: Overlay of the normalized polar angle distributions for coherent (solid) and incoherent (dashed).

bremsstrahlung intensities as functions of x and θ are combined into one probability density function, which is based upon the derivations in ref. [34]. We have not yet incorporated the effects of multiple scattering, crystal mosaic spread, nor incident electron beam divergence. We assume that the crystal radiator is a thin wafer of diamond, and that only the reciprocal lattice vector $(02\bar{2})$ contributes to the coherent bremsstrahlung spectrum. For a given x ($x \leq x_d$) and θ , then, the ratio of the intensities of the uncollimated coherent and incoherent bremsstrahlung photons is quantified by the Debye temperature of diamond. Because of its relatively high Debye temperature, diamond is the preferred crystal for coherent bremsstrahlung production.

In Fig. 26 we overlay the incoherent and coherent polar angle distributions ($dN/d\theta$ vs θ). One sees a clearly delineated band in the scatter plot of the total photon counts (coherent + incoherent) as a function of characteristic angle and fractional photon energy (Fig. 27). We then collimate the beam to reduce the incoherent background, which further serves to increase the degree of polarization (see Ref. [35]). The maximum polar angle is limited by the opening angle of the collimator θ_{coll} , which gives a lower limit for coherent bremsstrahlung

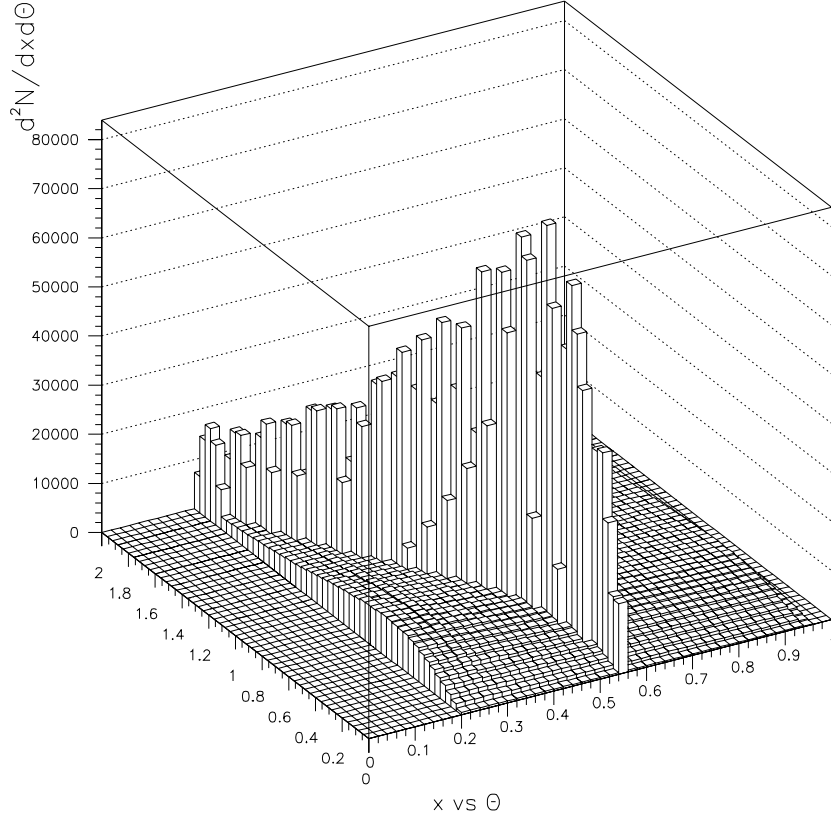


Figure 27: Number of photons per bin in fractional photon energy $x = k/E_o$ and polar angle in units of characteristic angle $[m_e c^2/E_o]$ for the sum of coherent and incoherent bremsstrahlung, here $x_{\max} = 0.55$.

photon energy

$$x_{\min} = \frac{x_d}{1 + \theta_{\text{coll}}^2(1 - x_d)}. \quad (21)$$

Therefore a spectral line in the energy region $x_{\min} \leq x \leq x_d$ remains for the collimated coherent bremsstrahlung photons. In Figs. 28a–d, we plot the total bremsstrahlung (coherent + incoherent) spectrum as a function of photon energy for four different collimator apertures overlayed upon the uncollimated spectra. And in Figs. 29a–d, the relative intensity for these four collimator settings, where we define

$$I_{\text{rel}} = \frac{I_{\text{coh}} + I_{\text{inc}}}{I_{\text{inc}}}, \quad (22)$$

and the intensity is proportional to $k \, dN/dk$. Finally, in Figs. 30a–d, we plot the degree

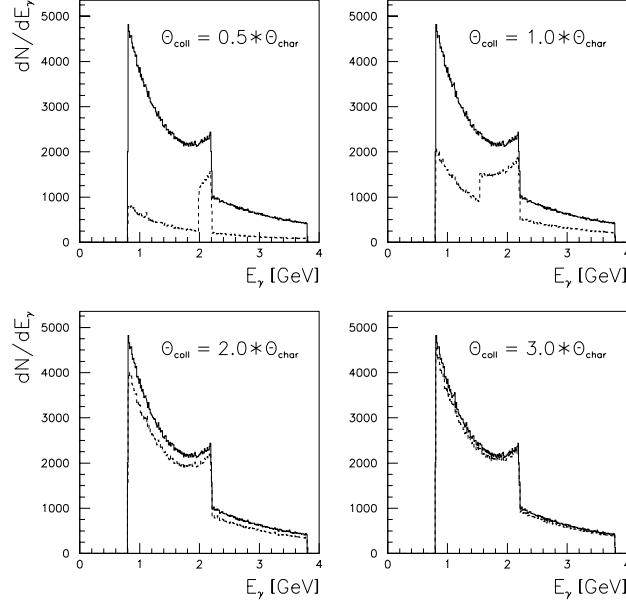


Figure 28: Superimposed coherent (dashed) and incoherent (solid) dN/dE_γ vs E_γ bremsstrahlung distributions under various collimator opening angles.

of linear polarization as a function of x under four collimator settings for $E_o = 4.0$ GeV. If we collimate the photon beam to $\theta_{\text{coll}} = \theta_{\text{char}}/2$ (θ_{char}), we will obtain average polarizations of 70% (65%) for $1.98 \leq x \leq 2.2$ GeV ($1.85 \leq x \leq 2.20$ GeV). Tightly collimating the beam to 0.125 mrad should be reasonably straightforward, since SLAC was able to survey a collimator of diameter 2 mm at 91 m ($\theta_{\text{coll}} = 11 \mu\text{rad}$) [36].

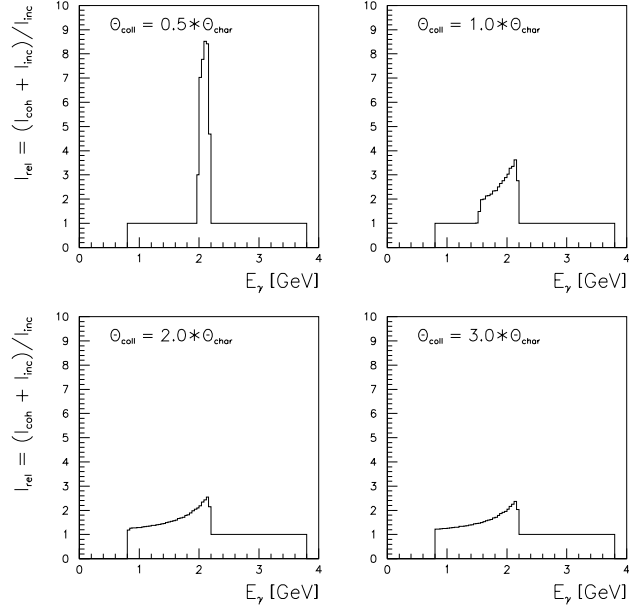


Figure 29: The relative intensity as a function of photon energy under various collimator opening angles. $I_{\text{rel}} = I_{\text{tot}}/I_{\text{inc}}$ and $I \propto E_\gamma \cdot dN/dE_\gamma$.

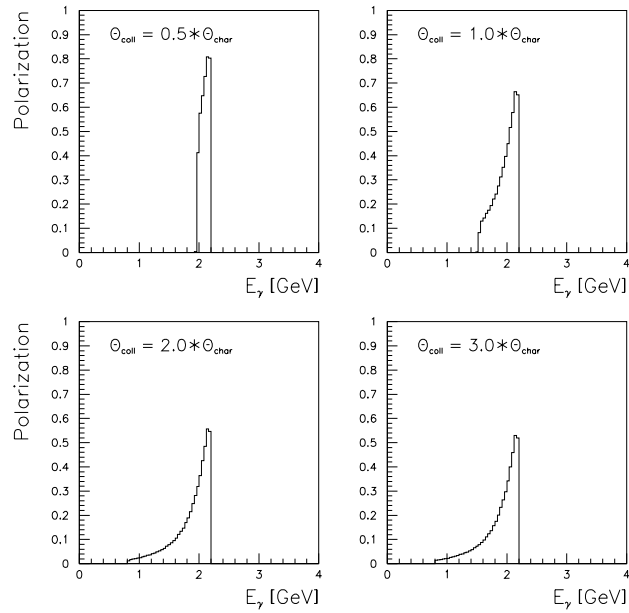


Figure 30: Polarization of coherent bremsstrahlung spectral line as a function of photon energy for various collimator opening angles.

5.2 Tagger Accidentals

We have performed a study to determine the usable tagging rate with a coherent bremsstrahlung photon beam. We define an accidental as any charged particle that registers a hit in a TOF counter that occurs within 10 nsec of the $\gamma p \rightarrow \omega p$ event. We have studied beam collimations of a characteristic angle with the coherent peak set at a maximum of $E_\gamma = 2.20$ GeV for an incident electron beam energy of 4.0 GeV. We assume the LH₂ target to be of length 14 cm. We performed the study under varying the following conditions:

- The overall CLAS acceptance (from 60 to 80%) for any $\gamma + p$ event.
- The minimum 3-momentum required for a final-state proton or pion to pass through all three drift chamber regions and register a hit in a TOF counter. We assume that the reaction $\gamma p \rightarrow p\pi^0$ is twice as likely to occur as the $\gamma p \rightarrow n\pi^+$ channel. The final-state particles were distributed uniformly in c.m. phase space by the CERNLIB routine GENBOD [27]. We then determined the likelihood that the momentum of the particle exceeded the cutoff value. We expect the momentum cutoff values to vary as a function of angle in the CLAS. Below are our ranges in cutoff momenta of the final-state proton and pion.
 - $|\vec{p}_{\text{prot}}| \geq 0.20$ GeV/c and $|\vec{p}_\pi| \geq 0.15$ GeV/c.
 - $|\vec{p}_{\text{prot}}| \geq 0.20$ GeV/c and $|\vec{p}_\pi| \geq 0.20$ GeV/c.
 - $|\vec{p}_{\text{prot}}| \geq 0.30$ GeV/c and $|\vec{p}_\pi| \geq 0.15$ GeV/c.
 - $|\vec{p}_{\text{prot}}| \geq 0.30$ GeV/c and $|\vec{p}_\pi| \geq 0.20$ GeV/c.
- The number of recorded triggers per second in the CLAS. We assume that the lifetime of the data acquisition system is on the order of 98%, hence the data acquisition rate (DAQ rate) is roughly identical to the trigger rate.

In Fig. 31 we plot the number of tagged photons striking the target after tight collimation as a function of CLAS acceptance for trigger rates between 0.5 and 1.5 kHz. We see that for an overall CLAS acceptance of 80% and trigger rate of 1 kHz, the number of tagged photons per second incident on the target is 4.23×10^6 Hz. This corresponds to a tagging rate of 2.04×10^7 Hz. In Figs. 32a–c we plot the percentage of accidentals per 10 nsec coincidence

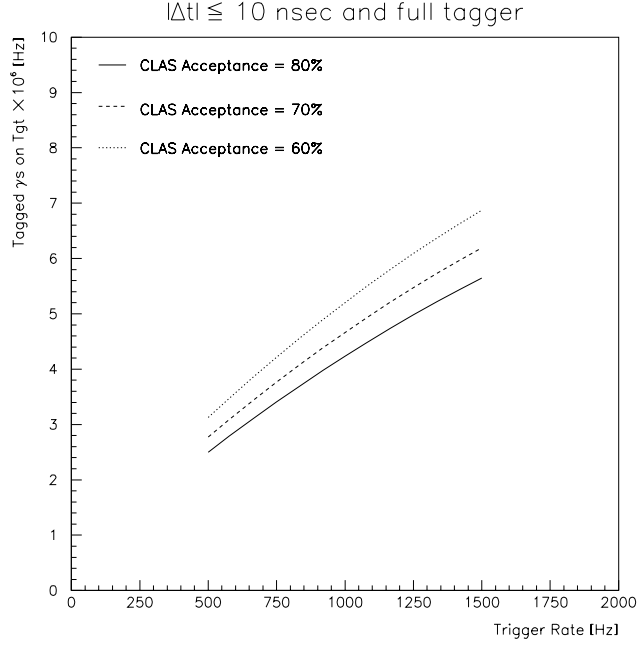


Figure 31: Collimated photons vs data acquisition rate as functions of the overall CLAS acceptance. We have set the collimation to one characteristic angle.

window versus CLAS acceptance as functions of both proton and pion momenta cutoff and trigger rate. We find for a trigger rate of 1 kHz, the percentage of accidentals to the total trigger rate is no worse than 33% with a CLAS acceptance of 80%.

With our conservative estimate of setting the coincidence window to 10 nsec, we expect then that the ratio of reals to accidentals to be *at the very worst* 2:1 for $E_o = 4$ GeV for a photon flux on target of $4.2 \cdot 10^6$ Hz with a DAQ rate of 1 kHz. As long as the accidental rate is low we will be able to separate the primary from the accidental events by means of energy balance in the offline analysis. We are investigating the option of tightening the coincidence window to 7 nsec, which will further reduce the accidental rate. Simply increasing the DAQ rate will serve only to increase the percentage of accidentals to real events, and will *not* serve to improve the collection of data, unless there is an accompanying tightening of the coincidence window.

$|\Delta t| \leq 10$ nsec and full tagger

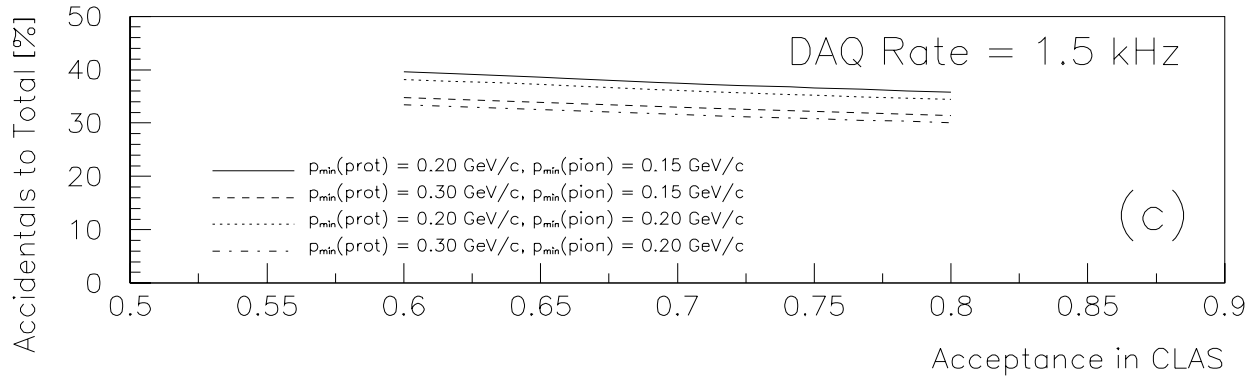
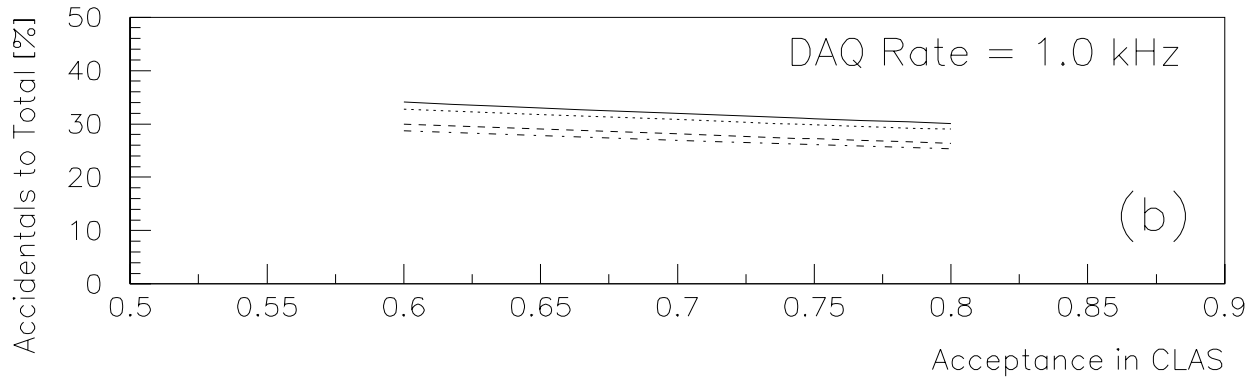
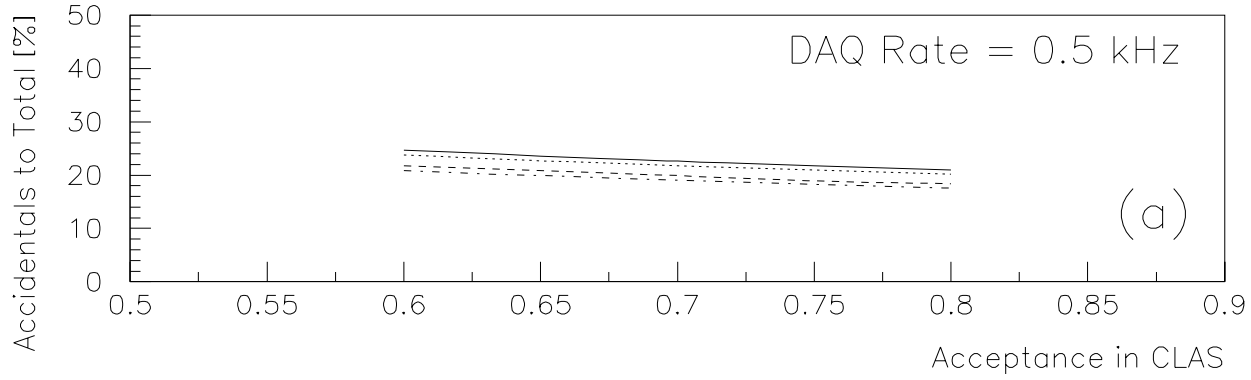


Figure 32: Percentage of accidentals vs the overall CLAS acceptance as functions of the cutoff momenta of the final-state protons and pions for three different data acquisition rates.

5.3 Count Rate Estimates

Data from Refs. [18] and [21] indicate that at photon energies below 2 GeV, the nondiffractive cross section of $\gamma p \rightarrow \omega p$ is $d\sigma/dt \simeq 2.0 - 2.5 \mu\text{b}/(\text{GeV}/c)^2$ in the four-momentum transfer squared range of $0.4 < -t < 1.0 (\text{GeV}/c)^2$. The anticipated number of ω events produced per second within this t range can be calculated from the formula

$$N_{\text{evts}} = \Phi N_{\text{nucl}} \frac{d\sigma}{dt} \Delta t \simeq 2.7 \text{ events/sec},$$

where Φ is the photon rate⁴, which is taken to be 4.5×10^6 Hz, $N_{\text{nucl}} = N_A \rho \tau$, $\rho \tau$ is equal to $(0.071 \text{ g/cm}^3)(14 \text{ cm})$, and Δt has been set to $0.6 (\text{GeV}/c)^2$.

Based upon our current studies and the acceptance studies for the Hall-B experiment E94-109, we will measure the c.m. polar angular region from $\theta_{cm} = 25^\circ$ to $\theta_{cm} = 145^\circ$; we expect the resonance photoproduction is most pronounced in the θ_{cm} region between 55° and 125° .⁵ Assuming an acceptance of 8–16 % for $N^* \rightarrow \omega p \rightarrow (\pi^+ \pi^- p) \pi^0$ in the photon energy range between threshold and 1.6 GeV, we should accumulate $\sim 7.5 \times 10^5$ ω events in a 20 day run. As the acceptance for these reactions increases to about 16–18% at higher photon energies ($1.5 \text{ GeV} < E_\gamma < 2.2 \text{ GeV}$) we expect to accumulate about 1.5 million ω events in a 25 day run. This will allow us to bin the data finely in \sqrt{s} and θ_{cm} as well as in the decay angles θ_{hel} and ϕ_{hel} . Because the count rate outside the central θ_{cm} region is 5 to 10 times greater, we will have sufficient statistics to extract the density matrix elements over $|\cos \theta_{cm}| < 0.8$ and hence over a wide range in t .

Such a high number of $p\omega$ events — several orders of magnitude greater than the current world's data set — will allow us to analyze the angular distribution of the decay pions for each bin in \sqrt{s} and θ_{cm} by extracting the ω signal within each bin in $\theta_{hel} \times \phi_{hel}$ separately.

⁴We have assumed that the linearly polarized beam of photons will be collimated to one characteristic angle.

⁵We will also be collecting data in the lower and higher $| -t |$ regions (i.e. $\theta_{cm} < 55^\circ$ and $\theta_{cm} > 125^\circ$).

5.4 Beamtime Request

This experiment has a natural link to experiments E94-109 [23] (Photoproduction of ρ Mesons from the Proton with Linearly Polarized Photons) and E98-109 [24] (Photoproduction of ϕ Mesons with Linearly Polarized Photons). Our proposed experiment will be using CLAS with the associated coherent bremsstrahlung facility and the same energy settings as the two already approved experiments. We will work closely with these collaborations, sharing the approved beam times of 11 days at 4 GeV electron energy and 22 days at 6 GeV beam energy. In order to perform an accurate analysis of $N^* \rightarrow \omega p$ in the c.m. energy range between 1.73 GeV and 2.24 GeV, we request an additional 400 hours of beamtime:

- 250 hours at 4 GeV electron beam energy to extract the density matrix elements at photon energies below 1.6 GeV;
- 150 hours at 6 GeV electron beam energy for the extraction of resonance contributions at photon energies above 1.5 GeV.

There will be 100 MeV overlap between these two data runs to provide for the cross checking of the systematics.

Below we list the experimental parameters.

Φ :	the photon flux ($4.5 \cdot 10^6 \gamma/\text{sec}$)
P_γ :	photon beam polarization: at least 60%
$\rho_{\text{LH}_2} = 0.071 \text{ g/cm}^3$:	density of liquid hydrogen
$\ell = 14 \text{ cm}$:	length of the Saclay cryo-target
B/B_o :	+0.5 (positively charged particles bending outwards)

References

- [1] Atkinson *et al.*, Nucl. Phys. B 231, 15 (1984).
- [2] J. Ballam *et al.*, Phys. Rev. D 7, 3150 (1973).
- [3] B. Fraas, Nucl. Phys. B 36, 191 (1972).
- [4] B. Friman and M. Soyeur, LNS/Ph/95-16, CNRS 1995.
- [5] D.B. Lichtenberg, Phys. Rev. 178, 2197 (1969);
R.E. Cutkosky and R.E. Hendrick, Phys. Rev. D 16, 2902 (1977).
- [6] R. Koniuk and N. Isgur, Phys. Rev. D 21, 1868 (1980);
N. Isgur and G. Karl, Phys. Lett. 72B, 109 (1977).
- [7] S. Capstick and N. Isgur, Phys. Rev. D 34, 2809 (1986).
- [8] S. Capstick and W. Roberts, Phys. Rev. D 47, 1994 (1993).
- [9] Particle Data Group, EPJ C 3, 623 (1998).
- [10] C.P. Forsythe and R.E. Cutkosky, Z. Phys. C 18, 219 (1983).
- [11] H. Funsten *et al.*, E91-024; Also refer to: V.D. Burkert, “Electromagnetic Excitation of Nucleon Resonances,” CEBAF-PR-94-005, the relevant list of approved N^* experiments is contained in Table 1 of this reference.
- [12] K. Schilling, P. Seyboth, and G. Wolf, Nucl. Phys. B 15, 397 (1970);
D. Schildknecht and B. Schrempp-Otto, Nuovo Cim. 5A, 103 (1971).
- [13] J.-M. Laget, “What can we learn from experiments with 10 GeV photons,” DAPNIA/SPhN_98_54;
J.-M. Laget and R. Mendez-Galain, Nucl. Phys. A 581, 397 (1995).
- [14] M. Pichowsky, C. Savkli, and F. Tabakin, Phys. Rev. C 53, 593 (1996); C. Savkli, F. Tabakin, and S.N. Yang, Phys. Rev. C 53, 1132 (1996); W.M. Kloet, W.T. Chiang, and F. Tabakin, Eprint nucl-th/9803042 (1998).
- [15] Q. Zhao, Z.P. Li, and C. Bennhold, Phys. Rev. C 58, 2393 (1998);
Q. Zhao, Z.P. Li, and C. Bennhold, Phys. Lett. B 436, 42 (1998).
- [16] S. Capstick and W. Roberts, Phys. Rev. D 49, 4570 (1994); W. Roberts, *Report to the GRAAL Group on Photoproduction of Baryon Resonances Using Polarized Photons* (1994), unpublished.
- [17] R.L. Anderson *et al.*, Phys. Rev. D, 679 (1976).
- [18] Aachen-Berlin-Bonn-Hamburg-Heidelberg-München Collaboration, Phys. Rev. 175, 1669 (1968).
- [19] CEA-Bubble-Chamber-Group, Phys. Rev. 146, 994 (1966).
- [20] Y. Eisenberg *et al.*, Phys. Rev. Lett. 22, 669 (1969).
- [21] F.J. Klein, Ph.D. thesis, Bonn-IR-96-008 (1996);
F.J. Klein, “Overview over Vector Meson Photoproduction,” πN Newsletters, No. 14, 141 (1998).
- [22] L.Y. Brovkin *et al.*, Phys. At. Nucl. 56, 762 (1993).
- [23] P.L. Cole, J.P. Connelly, R.R. Whitney, spokespersons, “Photoproduction of ρ Mesons from the Proton with Linearly Polarized Photons,” Jefferson Lab E94-109.

- [24] P.L. Cole, J.A. Mueller, D.J. Tedeschi, spokespersons, “Photoproduction of ϕ Mesons with Linearly Polarized Photons,” Jefferson Lab E98-109.
- [25] E.S. Smith, “FAST Monte Carlo for the CLAS Detector,” CLAS-NOTE 90-003; P.L. Cole, “A Generalized FASTMC for the CLAS,” CLAS-NOTE 93-006.
- [26] “Standard Data Analysis” by B. Niczyporuk.
- [27] CERN program library, CERNLIB 96A.
- [28] D.I. Sober, *private communication*.
- [29] W. Kaune *et al.*, Phys. Rev. D11, 478 (1975).
- [30] D. Lohman *et al.*, Nucl. Instr. Meth. A 343, (1994); J. Peise, M.S. Thesis, Universität Mainz (1989); D. Lohman, M.S. Thesis, Universität Mainz (1992); F. Rambo, M.S. Thesis, Universität Göttingen (1995); A. Schmidt, M.S. Thesis, Universität Mainz (1995).
- [31] F.H. Dyson and H. Überall, Phys. Rev. 99, 604 (1955); H. Überall, Phys. Rev. 103, 1055 (1956).
- [32] H. Überall, Phys. Rev. 107, 223 (1957); H. Überall, Z. Naturforsch. 17a, 332 (1962).
- [33] G. Diambrini-Palazzi, Rev. Modern Phys. 40, 611 (1968).
- [34] U. Timm, Fortschr. Phys. 17, 765 (1969).
- [35] R. Rambo *et al.*, Phys. Rev. C 58, 489 (1998).
- [36] C. Sinclair, *private communication*.